AN ABSTRACT OF THE THESIS OF

Benjamin C. Nielsen for the degree of Master of Science in Materials Science
presented on February 12, 2004.
Title: ANALYSIS OF THE PROCESSING AND CHARACTERIZATION OF *P*-TYPE $CuScO_2$ THIN FILMS

Abstract approved:

Dr. Janet Tate

Two different doping techniques, oxygen intercalation and Mg cation substitution, were investigated in thin film *p*-type $CuScO_2$, a wide band gap semiconductor with the delafossite structure. Films rf-sputtered onto amorphous SiO_2 substrates were polycrystalline after post-deposition annealing. X-ray diffraction was used to determine that the films are predominantly polycrystalline 3R $CuScO_2$ with 2H stacking faults, and that the formation of $Cu_2Sc_2O_5$ occurs at an intermediate processing stage. Oxygen intercalation increases the *a*-axis lattice parameter with a much smaller effect on the *c*-axis parameter. Mixed phases of oxidized and unoxidized $CuScO_2$ were observed in intercalated films. Substitution of up to 5% Mg for Sc increases conductivity to a maximum of 0.02 S/cm with no increase in optical absorption. Oxygen intercalation increases conductivity to a maximum of 26 S/cm with a significant increase in optical absorption. Grain growth and surface morphology changes after annealing were observed using atomic force microscopy. $CuScO_2$ deposited onto single crystal Al_2O_3 substrates at high temperatures using pulsed laser deposition were strongly *c*-axis oriented, and required no post deposition annealing. The conductivity was lower for the same oxygen intercalation treatment, indicating that grain boundary effects are important for diffusion of oxygen. Optical absorption of such films indicated a direct band gap of 3.6 eV.

© Copyright by Benjamin C. Nielsen
February 12, 2004
All Rights Reserved

ANALYSIS OF THE PROCESSING AND CHARACTERIZATION OF *P*-TYPE $CuScO_2$ THIN FILMS

by
Benjamin C. Nielsen

A THESIS

submitted to

Oregon State University

in partial fulfillment of
the requirements for the
degree of

Master of Science

Presented February 12, 2004
Commencement June 2004

Master of Science thesis of Benjamin C. Nielsen
presented on February 12, 2004.

APPROVED:

Major Professor, representing Materials Science

Head of the Materials Science Department

Dean of the Graduate School

I understand that my thesis will become part of the permanent collection of Oregon State University libraries. My signature below authorizes release of my thesis to any reader upon request.

Benjamin C. Nielsen, Author

ACKNOWLEDGEMENTS

The author expresses sincere appreciation to all the people who were instrumental in not only the completion of this thesis, but also in helping me get to this point in my life. First and foremost for my parents who gave me the opportunity to study and were a tremendous help emotionally and financially. Their continual encouragement and support has been crucial throughout my education and all my life experiences. To my sister Holly for her understanding and support in helping me follow my dreams. To my advisor, Dr. Janet Tate, for letting me participate in this project and for providing many long and insightful discussions and tutorials concerning my research. Thanks to all the members of my research group. Namely Robert Kykyneshi for assisting me with conductivity measurements and for being a great office mate, Matt Price for helping me with sputtering and various other facets of my research, Andrew Dreaseke and M.K. Jayaraj for establishing the research on $CuScO_2$ and originally introducing me to this material, Hiroshi Yanagi for his incredible knowledge of *p*-type transparent semiconductors, Paul Newhouse for preparing films with me on the pulsed laser deposition system, and all the others involved with Janet's research group. Joe Magner has been a tremendous help figuring out the seemingly constant problems with the sputterer and for his assistance with anything electrical and otherwise. Chris Tasker for his friendliness and enthusiasm, for showing me around the clean room, and for performing maintenance on the equipment. It was a pleasure to collaborate with Melinda Valencia. Thanks to Jun Li for her insight into this material and for showing me a few things around the lab. To Alex Yokochi for his help with X-ray analysis. I am thankful for what I

learned from the other professors involved with the TCO research including Dr. Wager, Dr. Keszler, and Dr. Sleight. Thanks to Dr. Bill Warnes for his friendly conversations and for making me an expert with MS Excel from all the homework assignments. Thanks to Joa Young Jung and Cheol-Hee Park for the good company over countless cups of coffee. And to Kevin who is not only a good roommate but also a great friend. I am sincerely grateful for all the professors and fellow students along the way who have helped me in many aspects and made my education interesting and fun.

My research was supported under the National Science Foundation (DMR 007127).

In retrospect, I can say with conviction that I have learned a great deal from my research. This is especially true seeing as how when I began graduate school over two years ago I knew almost nothing about these materials. I have developed a deep appreciation for how involved research can be. I have spent long periods of time just in figuring out how some equipment operates, and then on top of that there was the continuous occurrence of things not working the way you expect them to. I still have much to learn. I'm sure that if I wanted to I could have focused my entire thesis on a single facet of my project and researched it extensively. There are definitely parts of this study that I would have liked to spend some more time on. However, I am grateful for being exposed to different processes and equipment and receiving a broad overview of the research process. Perhaps most importantly, I feel that I have been given the necessary tools to conduct further scientific research.

TABLE OF CONTENTS

TABLE OF CONTENTS (CONTINUED)

LIST OF FIGURES

LIST OF FIGURES (CONTINUED)

LIST OF FIGURES (CONTINUED)

LIST OF TABLES

ANALYSIS OF THE PROCESSING AND CHARACTERIZATION OF *P*-TYPE $CuScO_2$ THIN FILMS

1 INTRODUCTION

This thesis project is concerned with the development of materials that are both transparent to visible light and conductors of electricity. This is indeed an unusual combination of characteristics since a material that conducts well, such as a metal, is usually opaque, and a transparent material such as window glass is usually an insulator. In the case of the metal, it appears opaque because all its free electrons are able to absorb and re-emit the energy of the incident photons. In the case of glass all its valence electrons are tightly bound together with the atoms in ionic bonds so they are not able to absorb the energy of the photons. As a result, the photons pass through the material and it thus appears transparent. Also, directly related to the fact the electrons are immobile is that the material is usually rendered an insulator. The idea behind this thesis is the exploration of the relationship between conductivity and transparency in materials, and determining whether or not a balance can be found between the two suitable for certain applications. More specifically, the modulation of conductivity and transparency using two different doping techniques is explored in *p*-type $CuScO_2$.

To achieve a desirable balance between conductivity and transparency in a material it must have both a wide enough band gap (> 3.1 eV) to transmit visible light

and enough mobile carriers to be conductive. The trick is to induce enough carriers in the material via doping without sacrificing its optical transparency.

Oxides generally have a wide band gap and are usually classified as insulators. This is due mostly to the ionic nature of the chemical bonds between metallic cations and oxygen anions. However, there are a number of oxides that can be made conductive through doping techniques. In semiconductors it is widely known that a material can be electron conducting (*n*-type), or hole conducting (*p*-type) depending on the dopant. Doping of zinc oxide, tin oxide, and indium oxide has been successful, and their conductivity can be improved substantially. This class of oxides is known as transparent conductive oxides (TCO). These materials may be deposited in the form of thin films using vacuum deposition techniques such as sputtering, evaporation, chemical vapor deposition (CVD), spray pyrolysis, or pulsed laser deposition (PLD).

N-type transparent conductors and semiconductors are well established and have been in industrial use for over 50 years. The first application was for defrosting windows on airplanes [1]. Today, the most common applications are in the transparent electrodes on flat panel displays and thin film photovoltaics, in touch screen displays, and in energy efficient low-emissivity windows in buildings. This market is dominated by just a few materials; tin doped indium oxide, In_2O_3:Sn, (ITO), fluorine doped tin oxide, SnO_2:F, and aluminum doped zinc oxide, ZnO:Al. ITO can be fabricated with a conductivity greater than 10^3 S/cm [2]. This is comparable to some metals, and yet ITO retains its high transparency of 85-90% in the visible spectrum. These materials remain transparent because they are degenerately doped at

shallow donor levels to carrier concentrations as high as 10^{21} cm^{-3}. Their band gaps are large enough so that the energy of visible light is too small to excite electrons from the valence band to the conduction band. As a result, absorption of visible photons is minimal.

Despite the fact that there are well-established *n*-type transparent conductors, no *p*-type transparent conductors or semiconductors of equivalent conductivity and transparency have yet been discovered. The current applications for TCO's are passive, and it is desired to find active applications. The advantage of finding reasonably conductive *p*-type transparent materials is in the fabrication of *p-n* junctions for use in active electronic or optoelectronic devices. The *p-n* junction is the basis of many electronic devices. A high-quality semiconductive *p*-type transparent material would result in the ability to construct transparent electronics. This could open the door for an array of new technology including transparent displays and photovoltaics. So for example, one could have a "heads-up" display in a windshield, or a window on a building could be an active solar cell. Indeed, the possibilities are endless if one could fabricate any electronic device using only transparent materials.

Recent research has led to advances in the area of transparent circuitry and the realization of some next generation optoelectronics. *P-n* junctions have been fabricated from materials such as *n*-ZnO/*p*-$SrCu_2O_2$ [3] and *p*-$ZnO{\cdot}Rh_2O_3$/*n*-$InGaZnO_4$ [4]. Very transparent thin film transistors have been made based on *n*-ZnO [5, 6, 7]. *P-i-n* heterojunctions have been constructed using a structure consisting of *p*-$CuYO_2$/*i*-ZnO/*n*-ITO [8]. *P-n* homojunctions have been made using $CuInO_2$, taking

advantage of the ability to bipolar dope this material with Ca to induce *p*-type conductivity and Sn to induce *n*-type conductivity [9, 10]. The devices utilizing *p*-type transparent semiconductors have displayed a lower than desired visible transparency and/or less than ideal electrical properties. However, the possibility exists that materials could be tailored to specific applications, and with the advances currently being made with *p*-type TCO's it is highly likely that better devices will be realized.

$CuAlO_2$ was the first reported *p*-type transparent semiconductor. The first report of *p*-type electrical properties in pressed powders of $CuAlO_2$ was by Benko and Koffyberg [11]. The birth of transparent electronics coincides with the first *p*-type transparent conducting thin films of $CuAlO_2$ reported by Kawazoe *et al.* [12, 13]. This material has the delafossite crystal structure, AMO_2, in which M is a trivalent metallic cation and A is a monovalent metallic cation. The delafossite structure is illustrated in Fig. 1.1. The crystal structure consists of close packed layers of MO_6 octahedra joined by relatively open Cu layers in O-Cu-O linear bonds. The name delafossite comes from the naturally occurring compound, $CuFeO_2$.

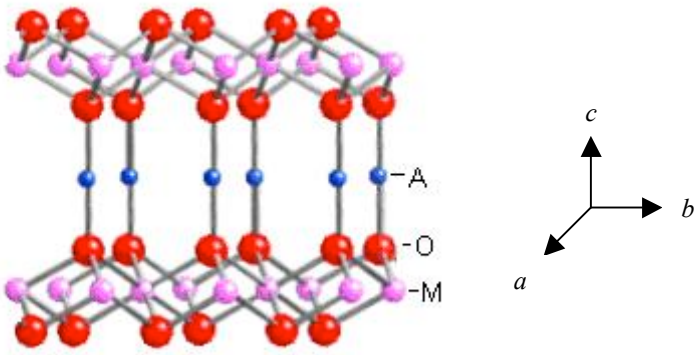

Figure 1.1 Delafossite crystal structure with the chemical formula $A^{+}M^{3+}O_2^{2-}$.

Since the report of *p*-type conductivity in $CuAlO_2$, a host of other Cu based delafossite materials have been reported with M=In [9, 10], Ga, Fe [14], Cr [15], Sc [16, 17], and Y [18]. Ag-based delafossite films have also been fabricated [14], although not as extensively as the Cu-based films. The reason the delafossite structure with A=Cu was thought to be a good candidate for *p*-type conduction is that the Cu^{1+} ion has a filled 3d orbital. The Cu^{1+} ion, with its $3d^{10}4s^0$ closed shell electronic configuration, is free from visible coloration from *d-d* transitions typically seen in transition metal ions [19].

The difficulty in doping many oxides to be *p*-type is thought to stem from the fact that the holes are localized at the valence band edge due to the strong electronegativity of oxygen. Also, the energy of the Cu $3d^{10}$ level is close to O $2p^6$. It was believed by Hosono and Yanagi *et al*. that this will result in some covalent bonding between these Cu and O levels so that the valence band spreads out and there is a decrease in the localization of holes [10, 19]. However, a paper by J. Li, A.W. Sleight, and A. Yokochi at Oregon State University reasons that the direct Cu-Cu interactions are responsible for hole conductivity, not the Cu-O interactions [26] so the covalent Cu-O bonding is not a factor. This coincides with the fact that the electrical properties are anisotropic due to the preferred conduction path of the holes lying along the copper planes in between the close packed layers. The anisotropic conductivity has been reported in research done on $CuAlO_2$ laminar crystals in which it was shown that the conductivity parallel to the *ab* planes is 25 times higher than the conductivity parallel to the *c* axis [20].

The conductivity can be improved substantially in some of the delafossites by incorporation of oxygen on interstitial sites [14, 16, 21, 22, 26]. The oxygen acquires two electrons from two adjacent Cu^{1+} sites to form O^{2-}. This effectively oxidizes the copper to Cu^{2+} and leaves empty states in the valence band to act as holes. Some delafossites are able to take up oxygen more easily than others. $CuAlO_2$ does not readily accept excess oxygen, whereas $CuScO_2$ will accept a significant amount up to $CuScO_{2.5}$ [26]. This is attributed to the larger size of the Sc^{3+} ion (0.745 Å) compared to the Al^{3+} ion (0.535 Å) [23]. The larger ion opens up the crystal structure so that oxygen can fit in more easily. It has been observed in $CuMO_2$ that the larger the M ion, the more oxygen that can be incorporated into the structure [22].

On the other hand, it is also desired that the Cu-Cu distance be short so that the hole transport is facilitated since the holes must hop from one Cu site to another. A short Cu-Cu distance also means oxygen intercalation will be more difficult. Fig. 1.2 shows the variation in lattice parameters of the rhombohedral $CuMO_2$ unit cell as a function of various M^{3+} ions. The larger ions extend the lattice parameters in the *a* direction, but not in the *c* direction. Intercalation is only possible when the M cation is Sc or larger. Sc is a logical choice for the M cation since it has the shortest Cu-Cu distance, and yet the structure is open enough so that it is still possible to intercalate.

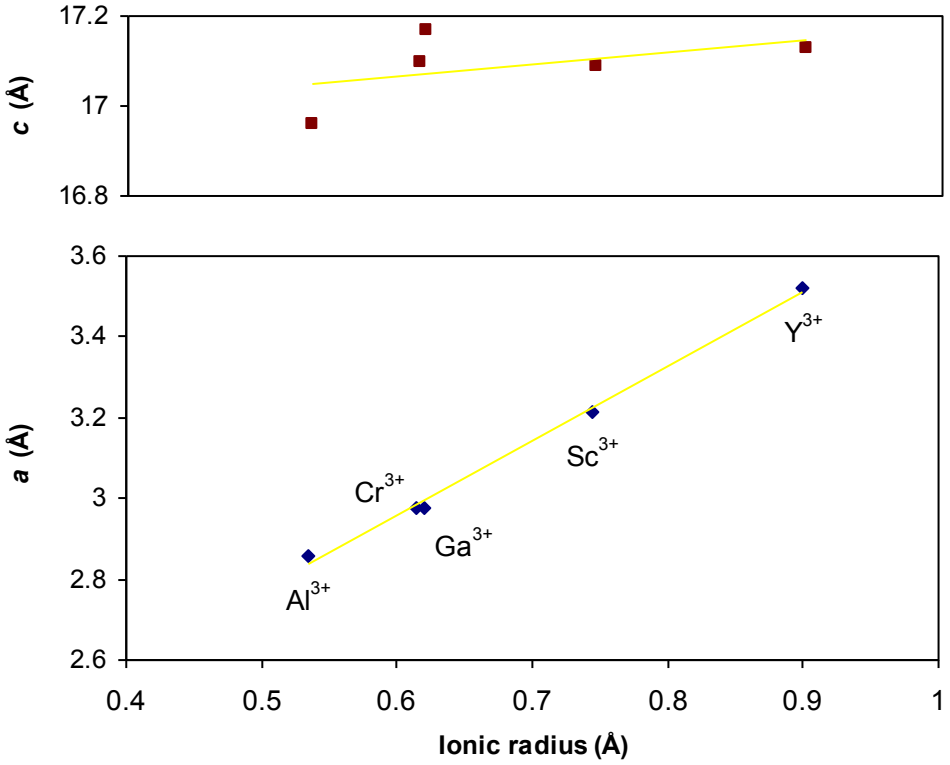

Figure 1.2 Variation of the *a* and *c* lattice parameters in 3R $CuMO_2$ as a function of various M^{3+} ions. M=Al, Cr, Ga, Sc, Y [23, 25].

The best conductivity in $CuAlO_2$ was reported as 1 S/cm [13]. With relatively heavy oxygen intercalation it was reported that conductivity was as high as 30 S/cm in $CuScO_2$ [16]. A conductivity of 220 S/cm was reported in $CuCr_{1-x}Mg_xO_2$ [15] (the highest for a *p*-type delafossite), and 1 S/cm in $CuY_{1-x}Ca_xO_2$ [18]. However, these films lose most of their transparency at these conductivities and show only 30-50% transmission in the visible spectrum.

This thesis project continues on the development of one specific delafossite material, $CuScO_2$. The research is a continuation of previous work that was done on this material system by A. Draeseke, M.K. Jayaraj, and others at Oregon State University [16, 17]. The processing conditions for sputtering and post-deposition

annealing that were used in the production of films for this project were established from the previous research. These parameters were used as a starting point for the work presented in this thesis. From the previous work it was shown that the conductivity could be drastically increased from the oxygen intercalation treatment. Fig. 1.3 shows the transparency of films as a function of conductivity. In these films, produced by A. Draeseke, various conductivities were obtained under different intercalation conditions. The highly resistive films are about 70% transparent in the visible spectrum (400-700 nm), and the most conductive films are only about 20% transparent. The most transparent (least conductive) films were intercalated at low oxygen pressures, and the least transparent (most conductive) films were intercalated at high oxygen pressures. All films were intercalated for 10 hours at 400°C. This

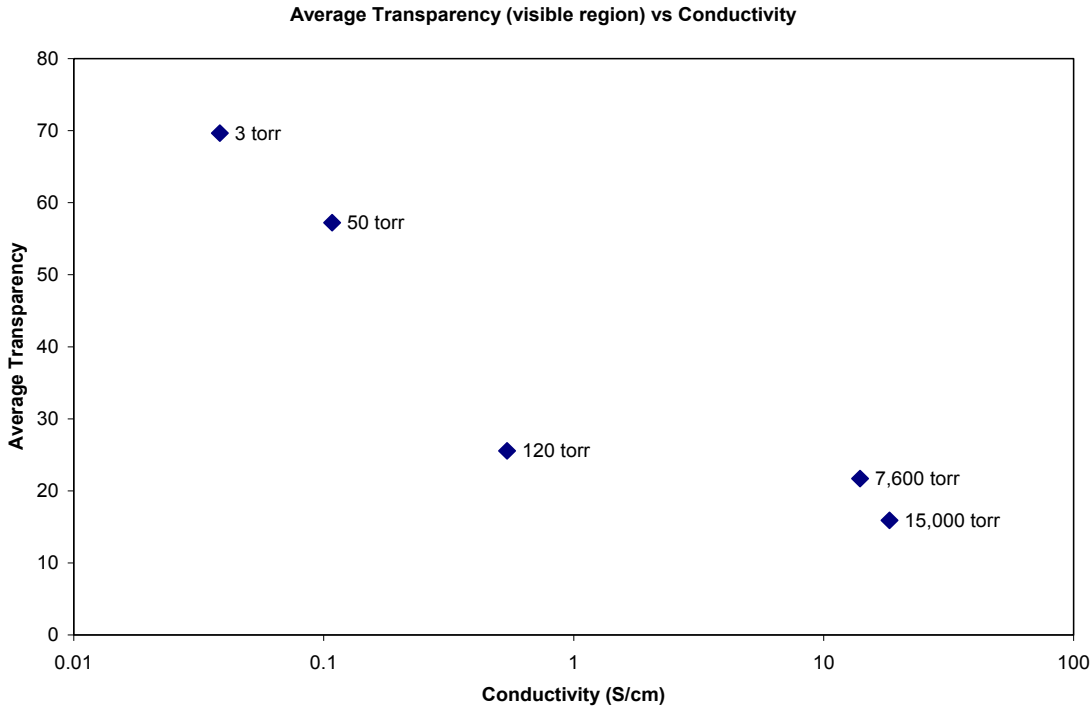

Figure 1.3 Conductivity vs. Transparency in $CuSc_{1-x}Mg_xO_{2+y}$ films. Films were intercalated at different oxygen pressures to obtain different conductivities.

temperature was chosen as the optimal temperature for intercalation because it is high enough for a reasonable intercalation rate, but low enough so that no phase transformations occur [27].

Doping of a Sc site with divalent cation also results in the creation of a hole and presents another technique for increasing carrier concentration. Magnesium was chosen as a dopant because it has a similar atomic radius to Sc (0.745 Å for Sc and 0.720 Å for Mg [23]) so the Mg should easily substitute for Sc. The oxidation states are Sc^{3+} and Mg^{2+} so a hole should be created upon substitution. However, in previous research it was not proven whether or not the Mg doping truly had an effect on the carrier concentration because all the films were made with an equal amount of Mg (~1.5 at% or less). The oxygen intercalation was always relied on to increase the carrier density. Doping levels in some TCO's are as high as 10%.

Additionally, it was not previously determined what effect the crystal morphology has on the overall properties. Presumably, the electrical and optical properties for a single crystal film will be significantly different than an amorphous film. Amorphous materials have a less defined band gap compared to their crystalline counterparts. In previous work films were deposited on glass at 350^{o}C substrate temperature and subsequently annealed. It was shown using X-ray diffraction (XRD) that the sputtered films were polycrystalline and generally *c*-axis oriented after post-deposition annealing. The choice of substrate of course has a large influence on the film characteristics. Amorphous glass substrates usually result in amorphous or polycrystalline films, and single crystal substrates result in films that are more crystalline or epitaxial. It is possible to deposit $CuScO_2$ on Al_2O_3 substrates since

both structures are hexagonal. There is a rather large lattice mismatch with a=4.24 Å for Al_2O_3 and a=3.22 Å for $CuScO_2$. This probably produces a strain in the film at the interface, or else the growing film can accommodate by growing in an off-axis direction.

$CuScO_2$ occurs in two different polytypes called 2H and 3R (space groups $P6_3/mmc$ and $R\bar{3}m$, respectively). The main difference between the two is that the alignment of the Cu sites repeats itself every other layer in the 2H polytype and every third layer in the 3R polytype, i.e. ABAB stacking for the 2H, and ABCABC stacking for the 3R. The 2H unit cell consists of only one close-packed layer, while the 3R unit cell consists of two close-packed layers. For this reason the c-axis lattice parameter is different for each polytype with $c_{3r}={}^3/_2 c_{2H}$=17.089 Å, while the a-axis lattice parameter is similar and is equal to about 3.22 Å. The difference between these two polytypes is illustrated in Fig. 1.4. There is also a phase that occurs at lower processing temperatures with a different stoichiometry, $Cu_2Sc_2O_5$. This phase has an orthorhombic structure with the copper existing as Cu^{2+} rather than Cu^{1+}. The material is insulating and greenish in color.

With the previously stated issues in mind, the goals of this project were to reproduce previous results, analyze the processing steps involved, and determine the effects of the magnesium doping and crystallinity. Transport, optical, and structural properties were measured after final and intermediate processing steps. In order to determine the effect of the Mg doping, three sputter targets were produced: undoped, 5% Mg doped, and 15% Mg doped. The results show that Mg doping is effective, but the oxygen intercalation increases the conductivity by a more substantial amount.

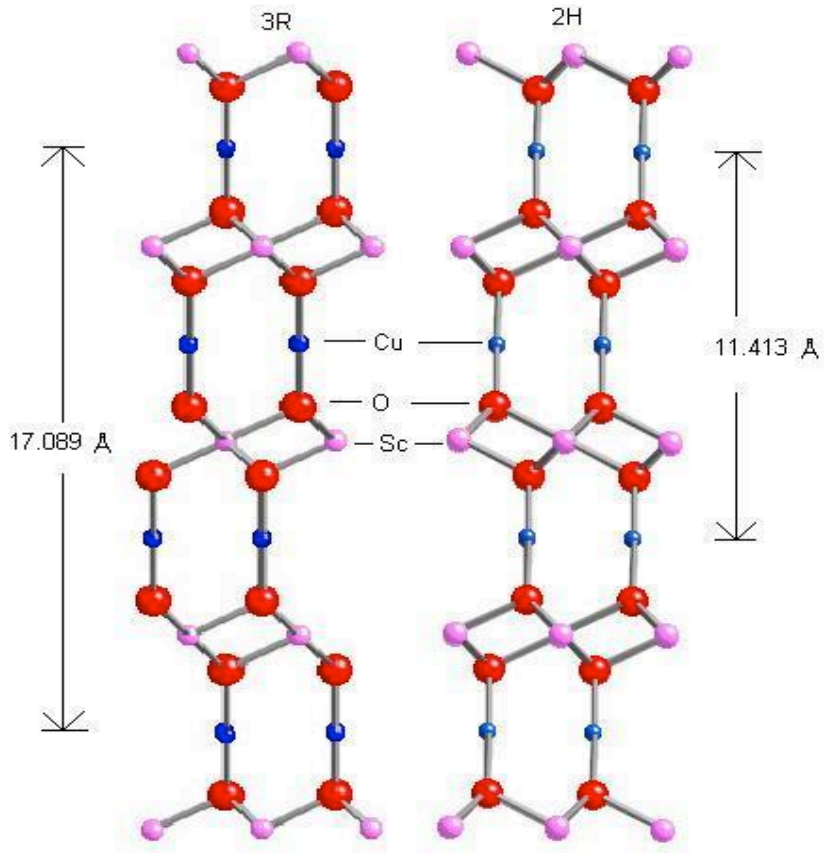

Figure 1.4 3R (left) and 2H (right) polytypes of $CuScO_2$.
In both phases a=3.22 Å, $c_{3R}={}^{3}/_{2}c_{2H}$.

It was also desired to see if there was an effect of crystal structure on the film properties. To determine the effect of crystal morphology, films were sputtered at various substrate temperatures from 100°C to 350°C. The sputter system used for this research only has the capability to heat the substrate up to ~500°C. Recently, a pulsed laser deposition (PLD) system was used to produce $CuScO_2$ films. This system allows substrate temperatures as high as 850°C so the possibility exists of producing epitaxial films on single-crystal substrates. Films were deposited on Al_2O_3 substrates and X-ray diffraction showed very high crystallinity, although not single crystal. These films were made from an undoped target, and after intercalation they

were not as conductive as the sputtered films. The polycrystalline films made via sputtering are more easily intercalated than the highly crystalline films made with the PLD. Thus grain boundaries must play a role in the intercalation process.

Each chapter in this thesis deals with a different facet of the processing and characterization steps. Chapter 2 describes the sputtering deposition process and the subsequent post-deposition film processing used in this research. Chapter 3 is devoted to various characterization techniques and the results of measurements performed on the sputtered films to determine their properties. These characterization techniques include X-ray diffraction, atomic force microscopy, electron microprobe analysis, conductivity, and optical analysis. Each subchapter begins with a brief description of the operation principles behind each characterization technique that is followed by details of the results. Chapter 4 discusses the results of the films made using the pulsed laser deposition system. These results are preliminary due to the fact that not enough time was available to conduct extensive research using this system. Nevertheless, analysis of the films does offer some interesting results. Chapter 5 provides an overall discussion of the major findings. Chapter 6 contains a conclusion, recommendations for future work, and a brief summary of new possibilities for *p*-type transparent semiconductors.

2 MATERIALS PROCESSING

2.1 Sputtering of Films

Films were produced using an rf-magnetron sputtering system. Rf sputtering is a vacuum deposition technique in which a radio-frequency (13.56 MHz)-induced electric field ionizes gas molecules to create a plasma. Rf sputtering is used as opposed to a dc sputtering when the target is a poor conductor to prevent charge depletion on the surface of the target. Argon is typically used as the sputter gas because it is heavy and inert, but in some cases reactive gases are used, for example when oxygen is to be incorporated into the film. Fig. 2.1 illustrates the sputtering process [24]. The plasma is magnetically confined to an area around the material being sputtered. Because the argon ions are positively charged they are attracted to the cathode on which the target material is mounted. The ions bombard the target and knock off atoms from the surface. Some of these atoms land on the substrate on which the film is to be deposited.

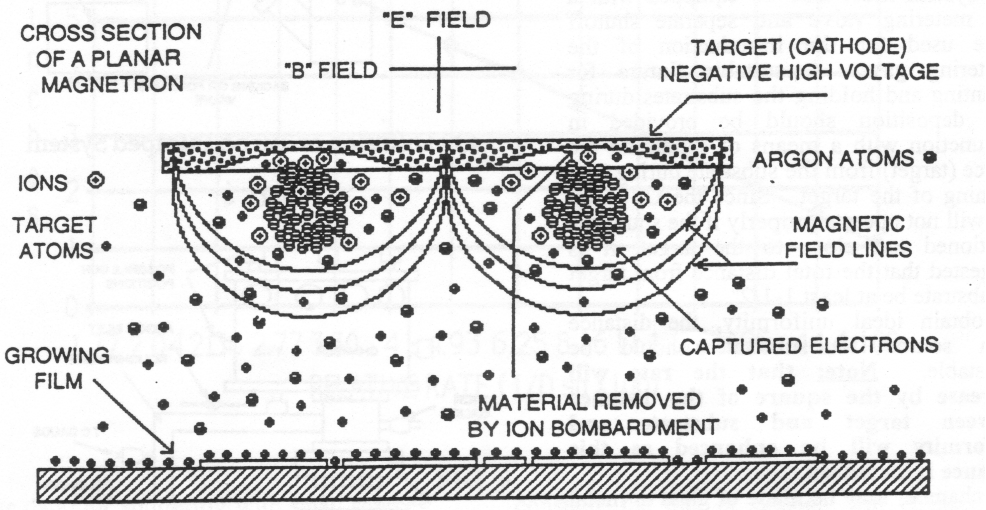

Figure 2.1 rf-Magnetron sputtering process as illustrated by the rf-magnetron gun manufacturer [24].

The first step, therefore, in the production of $CuScO_2$ films is to make a target of the material to be sputtered. For this thesis project three targets were produced of compositions $CuScO_2$, $CuSc_{0.95}Mg_{0.05}O_2$, and $CuSc_{0.85}Mg_{0.15}O_2$. The undoped target was produced to investigate the properties of the undoped material because in most of the previous studies at O.S.U. a Mg-doped target was used. The 5% Mg-doping level was chosen to compare to the undoped material and also to reproduce previous results. The motivation for a highly doped target was based on work done on the electronic properties of the bulk powder by J. Li and R. Kykyneshi at O.S.U. in which it was seen that the optimal conductivity occurred with a Mg-doping of about 5%. In relation to this, it was seen using electron micorprobe analysis (EMPA) that the processed films only contained about 1/3 of the Mg that was in the original target materials. These results are discussed in more detail in a later chapter. The 15% Mg-

doped target was produced with expectations that the final films would have about 5% Mg-doping.

The targets were disks 2" in diameter and between 1/8" and 1/4" in thickness. All targets were produced from the following powders: Cu_2O (Cerac 99+%), Sc_2O_3 (Stanford Mat. 99.999%), and MgO (Aldrich 99+%). It was found that a total mass of 30 g of powder produced a desirable sized target 2" in diameter and 0.15" in thickness. Powders were weighed using an electronic scale accurate to 10^{-4} g. A stoichiometric mixture of powder was first mixed by hand for 10 minutes until uniform. A mechanical mortar and pestle was used to grind the powder for 20 minutes. Then the powder was again mixed by hand for an additional 5 minutes. The powder was placed in a die and pressed uniaxially with 4 metric tons of pressure. The resulting pellet was placed on an alumina disk and put into a furnace. It was heated in air up to 1100^{o}C at 10^{o}C/min. It was held at that temperature for 24 hours then removed and quenched in air. Using this technique the $CuScO_2$ was synthesized according to the following reactions where (1) is for the undoped material and (2) is for the doped material.

(1) $Cu_2O + Sc_2O_3 \rightarrow 2CuScO_2$

(2) $Cu_2O + (1\text{-}x)Sc_2O_3 + 2xMgO + {}^{x}/_{2}O2 \rightarrow 2CuSc_{1-x}Mg_xO_2$

The targets were concurrently sintered during the compound synthesis from the furnace anneal to become relatively dense. The densities are given in Table 1 along with the percentage of the ideal single-crystal theoretical density of 4.574 g/cm^3 for

3R $CuScO_2$. The density is important because it influences sputter parameters such as uniformity and yield. Density can be improved up to 80% theoretical density by grinding, re-pressing, and re-sintering the powder.

Sputter Target	Density (g/cm^3)	% Theoretical
$CuScO_2$	2.42	53
$CuSc_{0.95}Mg_{0.05}O_2$	2.23	49
$CuSc_{0.85}Mg_{0.15}O_2$	2.57	56

Table 1 Sputter target densities. Measured densities are compared with the ideal 3R $CuScO_2$ single crystal density of 4.574 g/cm^3.

The sintered targets were mounted on a copper backing plate in order to achieve good electrical contact between the cathode block on the sputter gun and the target. The targets were bonded to the copper plates using a silver epoxy (Aremco Products). The epoxy was cured in air for 2 hours at room temperature, then at 90°C in air for 2 hours.

The target/mounting plate assembly was mounted on the rf-magnetron gun. The next step was to mount the substrate to be deposited on. Amorphous silica substrates were used for this experiment, however, single crystal substrates (usually Al_2O_3 for $CuScO_2$ since it has a similar crystal structure and lattice parameter) have also been used in order to achieve epitaxial films. Substrates used for this experiment were polished fused quartz from Technical Glass Products, Inc. The dimensions were 1"x1" and either 1/16" or 1 mm in thickness. First, the substrate was cleaned using a standard cleaning procedure of acetone, methanol, and de-ionized water (AMD). The

substrates were put in acetone in an ultrasonic cleaner for 2 minutes, rinsed with methanol, rinsed with DI water, and dried with a nitrogen gas jet. A substrate was mounted on a heater at a distance of 1.5" from the target in an on-axis configuration. An aluminum mask was used to mask part of the substrate off so that a thickness measurement could be made later, and also in some cases, so that the films could be patterned in various ways for certain applications. Both the mask and the substrate were held down flush against the substrate heater using an aluminum mask holder.

The sputter system used for this experiment consisted of a vacuum chamber that was pumped down to a base pressure of ~$5x10^{-7}$ Torr using a turbo-molecular pump backed by a belt driven mechanical pump. When the desired vacuum was achieved the chamber was filled with a flowing mixture of 36 sccm Ar and 0.54 sccm O_2 at a ratio of 100/1.5 to reach a steady deposition pressure of 12 mTorr. The rf power was turned on and ramped up to the operational power of 90 W over a period of 20 minutes. If a new target was being used, or one that had been exposed to atmosphere for an extended period of time, it was pre-sputtered for 12 hours. The substrate was heated to various temperatures ranging from 100^{o}C to 350^{o}C using a resistance heater. Different temperatures were used to determine the effect of crystallinity on the film properties. Lower temperatures result in a higher deposition rate, but with lower crystallinity in the films, and higher temperatures result in a slower deposition rate, but the films have a higher degree of crystallinity. This is because when atoms land on a very hot surface it is likely they will be re-evaporated unless they are in a stable, low energy position such as a lattice point in a growing film. In order to

improve uniformity a stepper motor was used to move the substrate holder and heater horizontally and vertically through the plasma.

Deposition times varied between 1.5 and 2.5 hours depending on the deposition rate and the desired film thickness. Films deposited at 150^{o}C required about ¾ of the time to obtain the same thickness as films deposited at 350^{o}C. Additionally, the film growth rate also depended on the target being used. The three sputter targets displayed a range of film growth rates even when all the deposition parameters were the same. This is because the targets were slightly different in thickness. The thickness of the target has a substantial effect on the sputter rate, and thus the film growth rate, because a thicker target results in less distance between the cathode (target) and the ground shield with the result being that the electric field is weaker. At 90 W with a 350^{o}C substrate temperature the thinnest target (15%Mg) that was 0.38 cm thick had the highest film growth rate of 0.031 nm/s, and the thickest target (5%Mg) that was 0.59 cm thick had the lowest film growth rate of 0.014 nm/s.

2.2 Post Deposition Processing

2.2.1 Measurement of Film Thickness and Etching

After deposition, the film thickness was measured using an Alpha Step 500 surface profilometer. With this technique, a small stylus is moved across the edge of the film and the vertical change between the substrate surface and film surface is measured. All the film thicknesses were measured to be between 50 and 250 nm. We

achieved repeatability with the measurements at best of about 10 nm. The 1 nm resolution claimed by the manufacturer was not achieved. Thickness varied depending on the target used during sputtering, the substrate temperature, the rf power, and the length of deposition.

Generally, thickness measurements of films evaporated through a shadow mask were reliable, but sharper edges can be achieved via photolithography and etching. For this purpose, and also for the purpose of patterning films for various applications it was necessary to find a suitable etchant. The films proved to be somewhat robust against typical etchants such as HCl and HNO_3, but an experiment revealed that undiluted 85% H_3PO_4 at 70^{o}C dissolved the films after about 2-4 minutes depending on film thickness.

2.2.2 Rapid Thermal Annealing

After deposition, the films are mostly, if not entirely, amorphous. In order to form polycrystalline $CuScO_2$ with fewer defects and greater transparency the films are put through an annealing process. After the thickness was measured the films were sequentially rinsed in acetone, methanol, and de-ionized water, and dried with a nitrogen jet before undergoing a 2-stage rapid thermal anneal (RTA). The furnace (AET Thermal RX) uses halogen lamps to heat films to high processing temperatures in only a few minutes with one complete cycle taking about 15 to 20 minutes. First they were heated to 750^{o}C at 500^{o}C/min. in 3 L/min flowing O_2, held for 2.5 minutes, and allowed to cool to ~200^{o}C over about 10 min. Then they were heated to 900^{o}C at

600^{o}C/min. in 3 L/min flowing Ar, held for 2.5 minutes, and cooled to room temperature in about 15 min.

2.2.3 Oxygen Intercalation

The final processing step is to intercalate oxygen into the films. After the RTA step the films are both highly transparent and very resistive. During the oxygen intercalation the films become much more conductive at the expense of transparency. A home-built tube furnace was used for the intercalation. Films were cleaned as before with acetone, methanol, and de-ionized water, and dried with nitrogen. The films were placed in a silica tube that was pumped down to a vacuum of ~1x10^{-6} Torr. The tube was then filled with O_2 to a pressure of 400 Torr. The apparatus was inserted into the tube furnace, heated to 400^{o}C at 10^{o}C/minute, held at that temperature for 9 hours, and quenched to room temperature. 400^{o}C was used because it is high enough for a reasonable oxygen diffusion rate, but not high enough to incur a phase transformation. It has been seen that there is a decomposition that occurs around 450^{o}C [26].

Additionally, a high pressure intercalation system was used to fully intercalate the films in order ascertain the maximum conductivity that could be achieved. This setup consisted of a stainless steel tube that the films were inserted into and then put into a tube furnace. Films were heated to 400^{o}C at 5^{o}C/minute, held at 800 p.s.i. (4x10^{5} Torr) O_2 for 24 hours, and cooled to room temperature at 10^{o}C/minute.

The films change significantly during the post-deposition annealing and intercalation processes. Fig. 2.2 shows pictures of the films after each of the

processing steps. The text underneath the films in Fig. 2.2 is clearly visible. The as-deposited film (A) appears brown and is insulating. After the O_2 RTA the film appears yellow-green and is insulating (B). After the Ar RTA (C) the film has its highest transparency and is a light blue-pink color. The films are conducting after this step, although with a low conductivity of about 10^{-5}-10^{-2} S/cm, and there is a large difference in conductivity between the undoped and Mg-doped films. After the intercalation (D), the film darkens somewhat to a shade of gray and the conductivity is improved by up to 3 orders of magnitude for the doped films and up to 6 orders of magnitude for the undoped films (1-30 S/cm). The changes in the crystal structure and phase formations after each processing step are discussed in the following chapter on X-ray diffraction, and further characterization is presented in subsequent chapters.

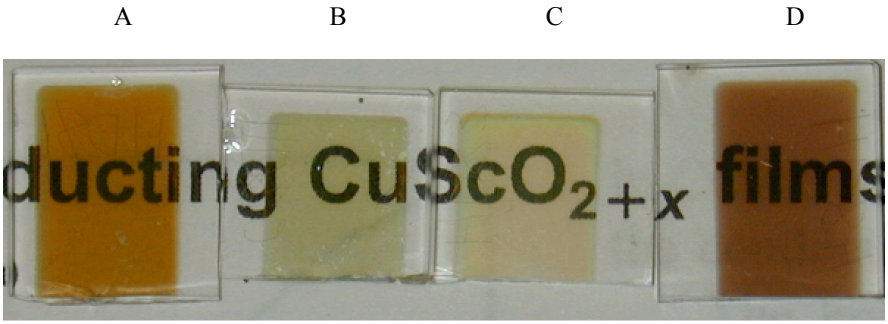

Figure 2.2 Appearance of films: (A) as-deposited, (B) after O_2 RTA, (C) after Ar RTA, and (D) after oxygen intercalation. The films are most transparent after annealing (C), then become darker from the intercalation (D).

3 CHARACTERIZATION DATA AND RESULTS

3.1 X-Ray Diffraction

3.1.1 Introduction

X-ray diffraction (XRD) gives information about the phases present in a material, crystallinity, and orientation of crystallites by measuring the intensity of a diffracted beam of monochromatic X-rays [28]. All crystals have a unique diffraction pattern because of the arrangement of the atoms and the spacing between crystal planes. X-rays diffract according to the Bragg equation, $\lambda=2d\sin\theta$, where λ is the wavelength of the radiation (typically, Cu Kα radiation, λ=1.5406 Å, is used as the X-ray source), d is the plane spacing, and θ is the angle of incidence of the X-rays with the planes. It is relatively straightforward to get reliable data from powder specimens because there are many randomly oriented crystallites and some will assuredly be aligned to satisfy the Bragg conditions. Films can prove more difficult to measure because they can be very thin, and also because they can be fully or partially amorphous, polycrystalline, epitaxial, or preferentially oriented. In this experiment, XRD was used to confirm both the synthesis of the powder used in the sputter target preparation and the film crystal structure.

3.1.2 Sputter Target Data

Fig. 3.1 shows the powder diffraction patterns obtained from the undoped, 5% Mg doped, and 15% Mg doped sputter targets. A Siemens D-5000 diffractometer was used to collect the data for 30 minutes at 2 degrees per minute while the sample was rotating.

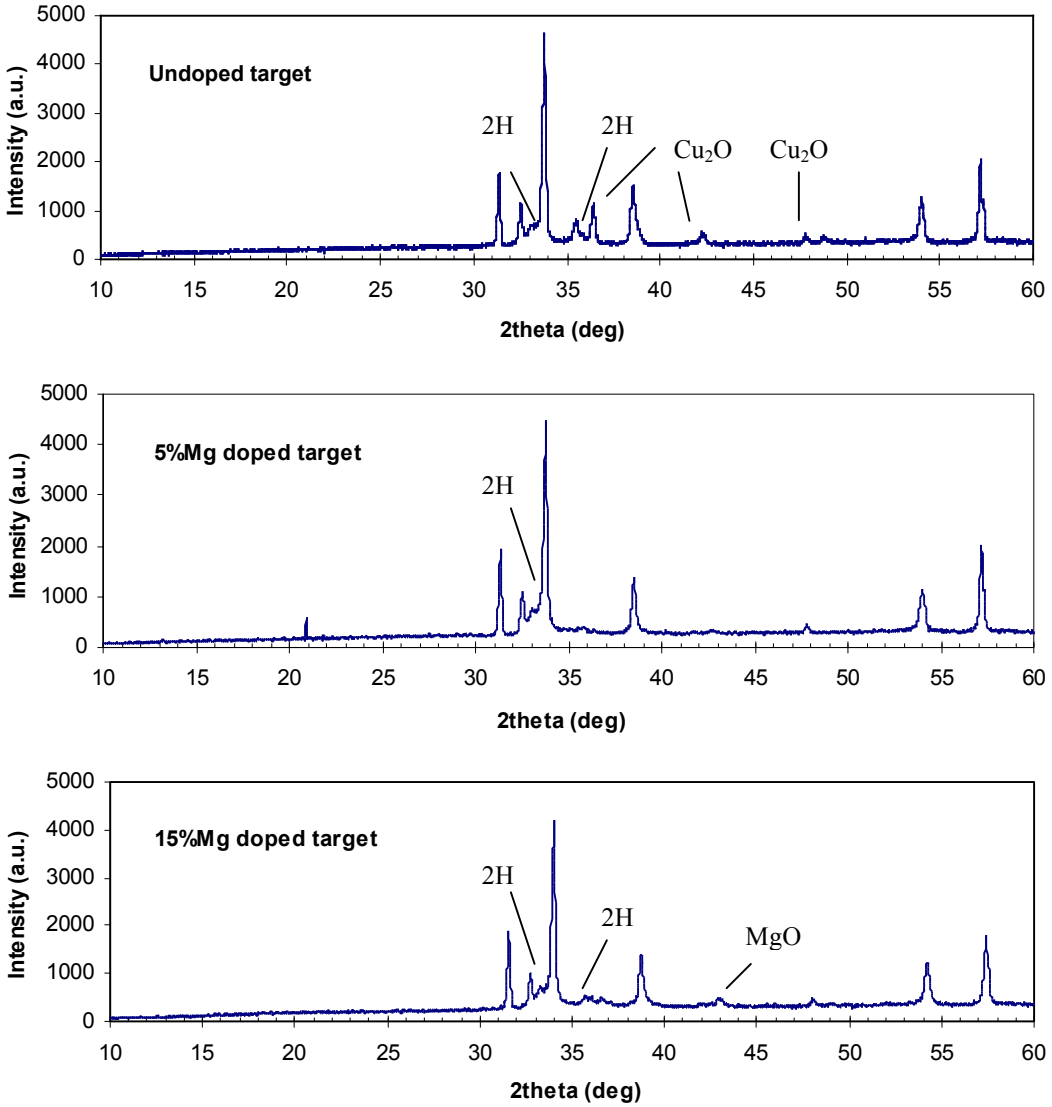

Figure 3.1 XRD patterns for $CuScO_2$, $CuSc_{0.95}Mg_{0.05}O_2$, and $CuSc_{0.85}Mg_{0.15}O_2$ sputter targets. The 2H phase and the Cu_2O and MgO impurity peaks are labeled. All other peaks are 3R.

These plots can be compared to the ideal single crystal diffraction patterns shown in Fig. 3.2 for the 2H and 3R phases of $CuScO_2$ and in Fig. 3.3 for the $Cu_2Sc_2O_5$ phase [25]. All the major peaks from the targets can be indexed to the 3R polytype of $CuScO_2$, but there is a presence of the 2H polytype in the targets, and there are some minor impurity peaks to note. Each target has a small amount of the 2H polytype, with the undoped target having the most. The undoped target has a small amount of Cu_2O. The 5% Mg target has the least amount of 2H and no impurity peaks and thus appears to be the most pure. There is a small presence of the 2H polytype and the Cu_2O impurity in the highly doped target, but it is not as high as in the undoped target. The only 2H peaks present in any of the three are from the most intense peaks from the ideal pattern in Fig. 3.2, the (*101*) and (*102*) lines. Additionally, the 15% Mg target shows a small impurity peak from MgO suggesting that the Mg could be reaching the solubility limit in the material.

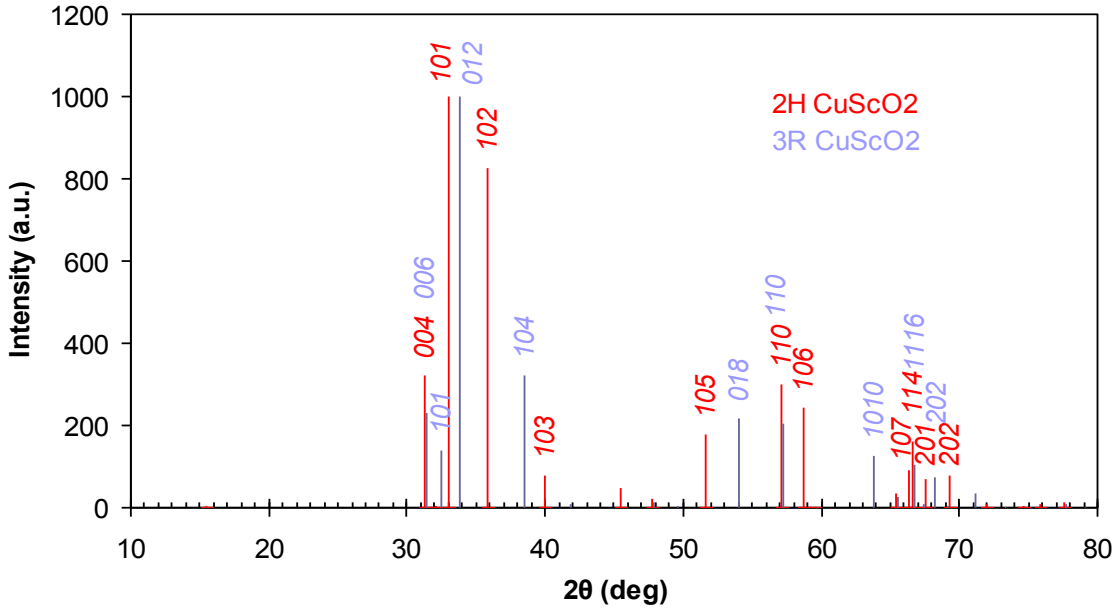

Figure 3.2 Theoretical diffraction patterns for 2H and 3R $CuScO_2$ with major *hkl* planes labeled. Data generated from JCPDS files [25].

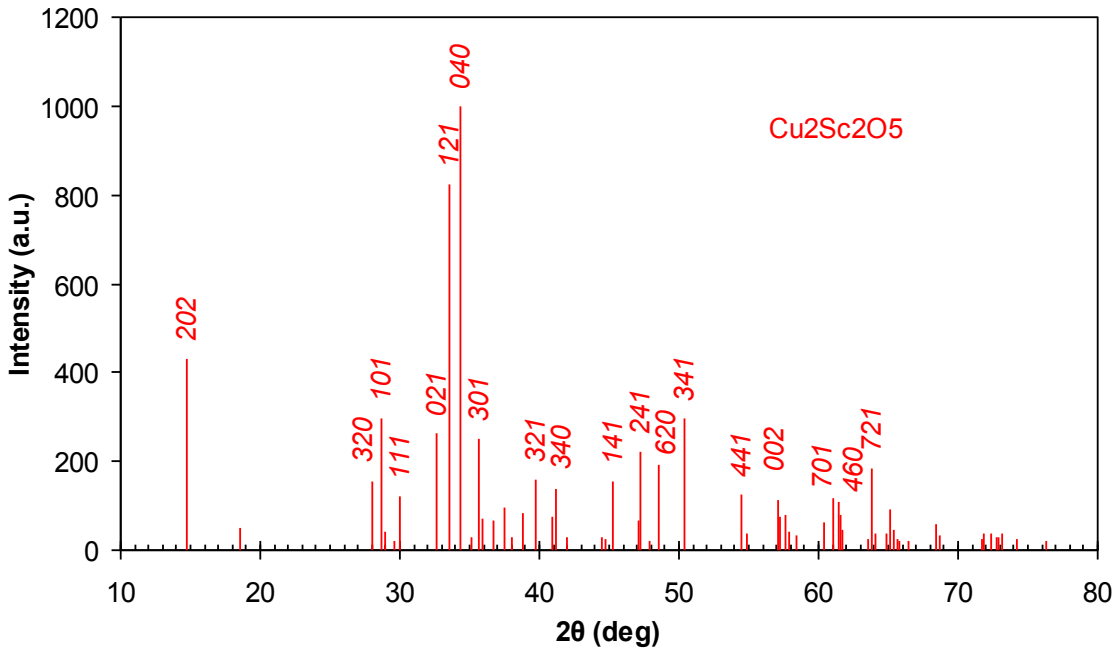

Figure 3.3 Theoretical diffraction patterns for $Cu_2Sc_2O_5$ with major *hkl* planes labeled. Data generated from JCPDS files [25].

3.1.3 Film Data

XRD was also used to characterize the films using a different diffractometer better designed for film analysis. Fig. 3.4 shows the plots obtained for the films after each processing step using a Rigaku Rapid rotating anode diffractometer with a curved image plate detector. With this setup, a low angle of incidence is used of $\alpha=9.5^{o}$-10^{o} and all diffracted X-rays are detected simultaneously. A cubic spline method was used to remove the background signal.

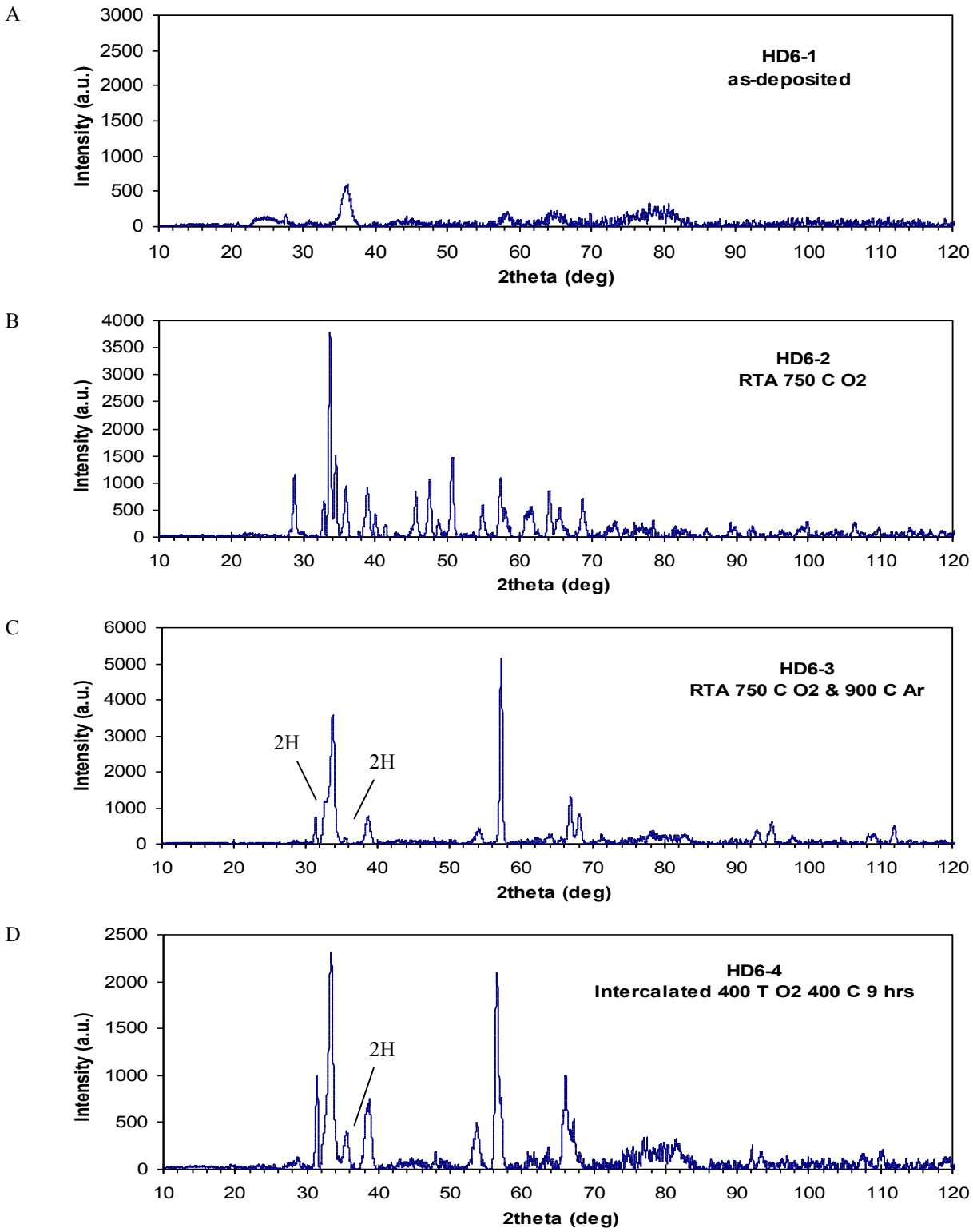

Figure 3.4 XRD plots for $CuSc_{1-x}Mg_xO_2$ films made from the 15% Mg target after each processing step. (A) is mostly amorphous, (B) is all $Cu_2Sc_2O_5$, in (C) and (D) all peaks correspond to 3R $CuScO_2$ with only a small amount of 2H $CuScO_2$ present.

The as deposited film (A) is almost completely amorphous. There is one noticeable peak around 2θ=36° that is close to the (*102*) 2H peak, but there are no other discernable 2H peaks such as the more intense (*012*) peak so it is doubtful that it is actually crystalline 2H. There are some remnants of maybe two or three other peaks, but they are very small. The main peak could be a conglomeration of reflections from the 3R and 2H polytypes, and even the 2-2-5 phase. Even though the crystal structure is amorphous the nearest neighbor distance is somewhat similar to the crystalline phase, giving some resemblance of structure. The XRD pattern of the film after the 750°C oxygen anneal (B) indicates that the film is polycrystalline and every peak can be indexed to $Cu_2Sc_2O_5$. After this step, the films turn from brown to a light green-yellow hue and are completely insulating. In the reduction in argon at 900°C Cu^{2+} is reduced to Cu^{1+} and the $CuScO_2$ crystallites nucleate and grow. In the pattern from this film (C) every peak can be indexed to the 3R phase of $CuScO_2$ except for one peak around 35.6° that can be attributed to a small presence of the 2H polytype. The films become significantly more transparent after this stage and usually have a light blue-pink hue. The undoped films remain insulating, but the Mg doped films have a small but measurable amount of conductivity (10^{-3}-10^{-2} S/cm). The intercalated film (D) shows all the same 3R peaks as seen in the third film, however, there is a slightly increased amount of 2H as evidenced by the more intense 2H peak.

No information can be gained from this data as to whether the films are preferentially oriented. Looking at the patterns in Fig. 3.4 it appears that the (*110*) peaks are the most intense. Comparing these to the JCPDS patterns in Fig. 3.2, the

(*110*) peaks should not be nearly as intense as the (*012*) peaks. This might be suggestive of the films being oriented in the *a* direction, however, this is not the case. This is because of the manner in which the raw data is integrated to get a *2θ* vs. *Intensity* plot. The intensities of the higher angle peaks are disproportionately large and are more intense than they should be. Problems with the data processing are currently being resolved.

One feature of the intercalated pattern of importance is that some peaks, more notably the higher angle (*110*) peak that is normal to the *c*-axis at $2\theta \approx 57.3^{o}$, but also the couplet of (*116*) and (*202*) peaks at $2\theta \approx 66^{o}$-68^{o} and the (*012*) peak at $2\theta \approx 33^{o}$, have shifted to smaller angles. This is clearly illustrated by overlaying the non-intercalated and intercalated XRD patterns as shown in Fig. 3.5. The shift

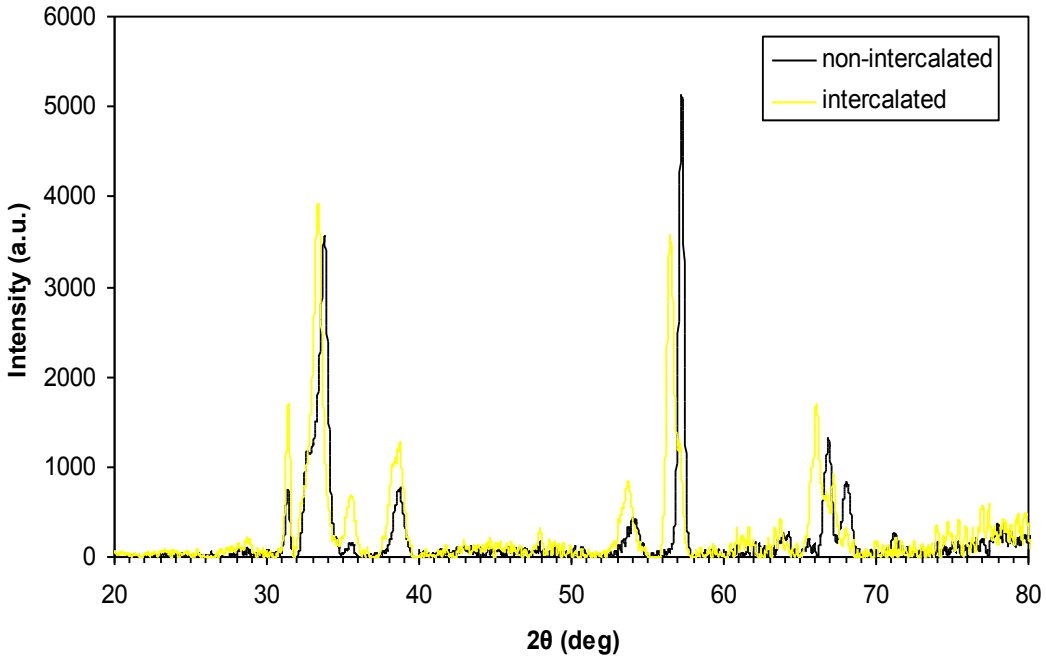

Figure 3.5 Comparison of X-ray patterns for the non-intercalated and intercalated $CuSc_{1-x}Mg_xO_{2+y}$ films. The splitting of the peaks into lightly and heavily doped phases and the shift to lower *2θ* is evident due to an expansion of the *a* lattice parameter with intercalation.

corresponds to a lattice expansion due to the extra oxygen uptake by the film during the intercalation process. Intercalated oxygen sits on interstitial sites within the lattice located between the close packed layers near the Cu sites. The oxygen causes an expansion of the *a* lattice parameter, but it has only a small effect on the *c* lattice parameter. This is because the close-packed MO_6 layers become distorted and make room for the extra oxygen by rotating and elongating in the *a*-direction while maintaining the same *c*-spacing [26]. The peaks are shifted because if the distance between planes, *d*, increases, the angle at which the X-rays diffract, θ, must decrease according to $\lambda=2d\sin\theta$.

The peaks that have shifted over have an *a*-axis lattice parameter of 3.26 Å. The non-intercalated films show an *a*-axis lattice parameter of 3.22 Å, the same value given in the JCPDS data [25]. The *c*-axis (*006*) peak has not moved from the pre-intercalated position, verifying that there is no change in the *c*-direction.

It is also seen in Fig. 3.5 that in the peaks that have shifted over to smaller 2θ a remnant peak of the original pre-intercalated position can also be seen. This splitting of the peaks is caused by the intercalated material actually segregating into a lightly doped phase and a heavily doped phase. This corresponds to similar trends seen in research done on the bulk powder form of $CuScO_{2+y}$ in which the intercalated material splits into a non-intercalated $CuScO_{2.0}$ phase and a heavily intercalated $CuScO_{2.5}$ phase with an *a*-axis lattice parameter of 3.26 Å [26].

There was also an intermediate peak found in a different set of films shown in Fig. 3.6 in which the *a*-axis lattice parameter was determined to be 3.24 Å. The films are non-intercalated, intercalated under low pressure, and heavily intercalated. The *a*-

axis lattice parameter in the heavily intercalated film was 3.26 Å. This corresponds to the previous value for the intercalated film in the other set. The splitting is seen in all the intercalated peaks that have shifted over with a small shoulder remnant of the original, pre-intercalated position. It is likely that the intercalated phase in the intermediate peak has not been fully oxygenated, or maybe just the surfaces of the crystallites have been oxygenated.

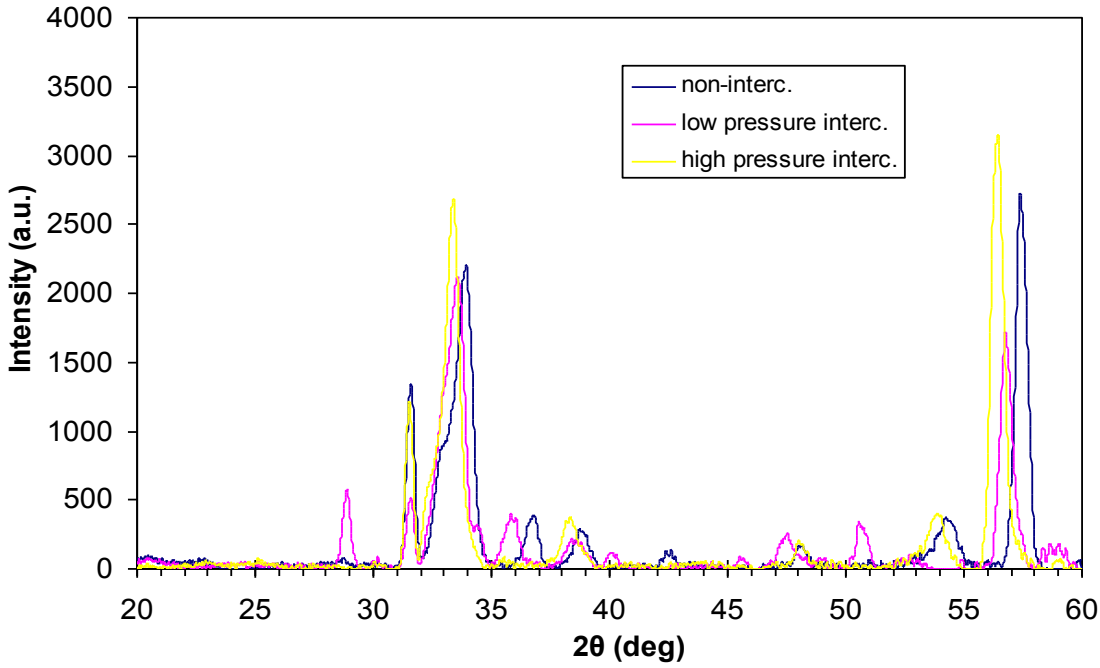

Figure 3.6 XRD patterns for non-intercalated, low pressure intercalated, and high pressure intercalated $CuScO_{2+y}$ films. An intermediate peak is observed between the lightly and heavily oxygenated phases.

The films become substantially more conductive from the intercalation at the expense of transparency. Interestingly, the intercalation treatment does not alter the phase of the material. There is an expansion in the *a* lattice constant, but the material remains isostructural with the 3R phase that existed before the intercalation. This is because the temperature at which the intercalation is done at (400^{o}C) is not high

enough to cause a phase transformation. Attempts were also made to intercalate the $Cu_2Sc_2O_5$ phase without any success. It is evident that this crystal structure cannot incorporate excess oxygen.

3.1.4 Conclusion

It was shown using X-ray diffraction that the sputter targets are mostly 3R $CuScO_2$ with a small amount of 2H $CuScO_2$ and minor impurities. XRD was used to ascertain the phase formation at the different stages of film processing. As-deposited films are amorphous. It was shown that one way to obtain $CuScO_2$ films is to first go through the $Cu_2Sc_2O_5$ phase. After the RTA in O_2 at 750^{o}C, polycrystalline $Cu_2Sc_2O_5$ forms and the films are a clear yellow-green color. After the RTA in a reducing Ar environment at 900^{o}C, polycrystalline 3R $CuScO_2$ forms with a small amount of the 2H polytype and the films are highly transparent. After intercalation of oxygen at 400^{o}C for 9 hours the films remain isostructural with the pre-intercalated films, but darken and become more conductive. The uptake of oxygen results in a splitting of the peaks that are not parallel with the *c*-axis into a lightly intercalated phase at the same 2θ as the peaks in the non-intercalated films and a heavily intercalated phase at lower 2θ. The *a*-axis lattice parameter is extended from 3.22 Å to 3.26 Å due to the distortion of the crystal structure. The *c*-axis lattice parameter remains unchanged after intercalation. An intermediate peak corresponding to an *a*-axis lattice parameter of 3.24 Å was also seen for a film that was intercalated at low oxygen pressure with the splitting still evident.

3.2 Atomic Force Microscopy

3.2.1 Introduction

Surface features are critical in thin film electronic materials because they influence physical characteristics and performance. If a film has a rough surface it will be unsuitable for use in a layered structure where interface quality is crucial. A poor interface in a device such as a *pn* junction will result in degraded or non-uniform transport properties due to an inhomogenous interface and surface defects.

To observe the surface morphology of the films and to get an estimate of the grain size, the surfaces of films were mapped using atomic force microscopy (AFM). This research used a Digital Instruments MultiMode Scanning Probe Microscope in contact AFM mode. AFM uses an atomically-sharp silicon nitride tip that moves back and forth across the film surface and detects changes in topography. The height variation data is given as either a 2-D or 3-D contour plot. For this project, a 1x1 μm size area was scanned at 2.977 lines/second and 256 lines/area.

3.2.2 Results and Discussion

Figs. 3.7-9 show AFM images for the films after each of the processing steps. The films were produced by A. Draeseke in an earlier experiment.

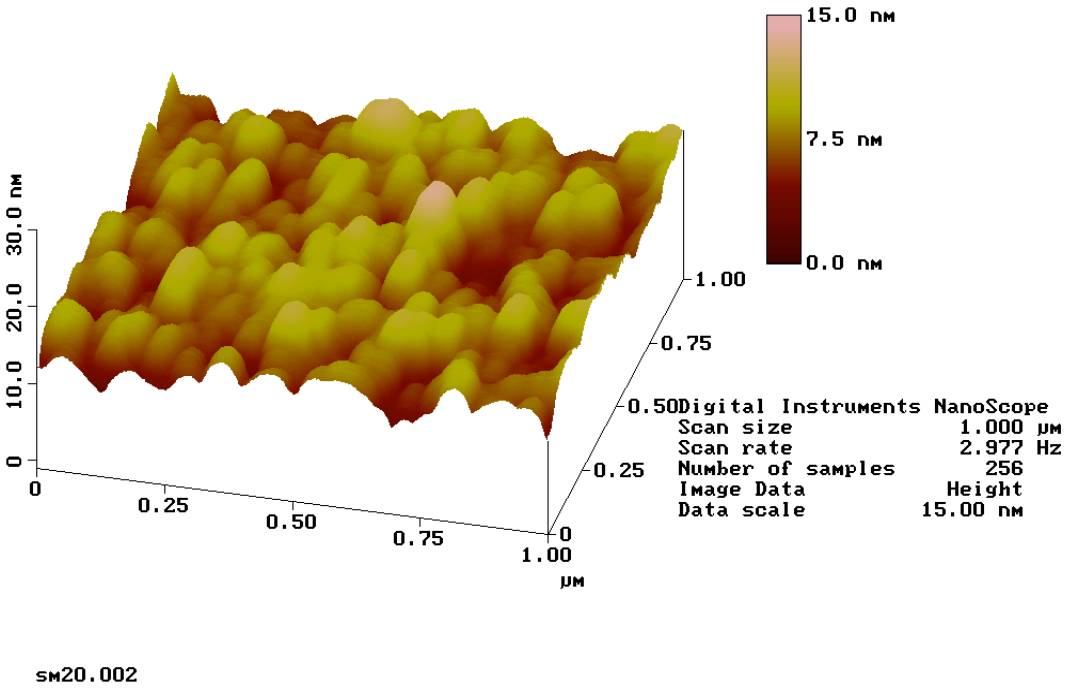

Figure 3.7 AFM image of as-deposited $CuScO_2$ film. Rmax=11.3 nm, Rms=1.6 nm.

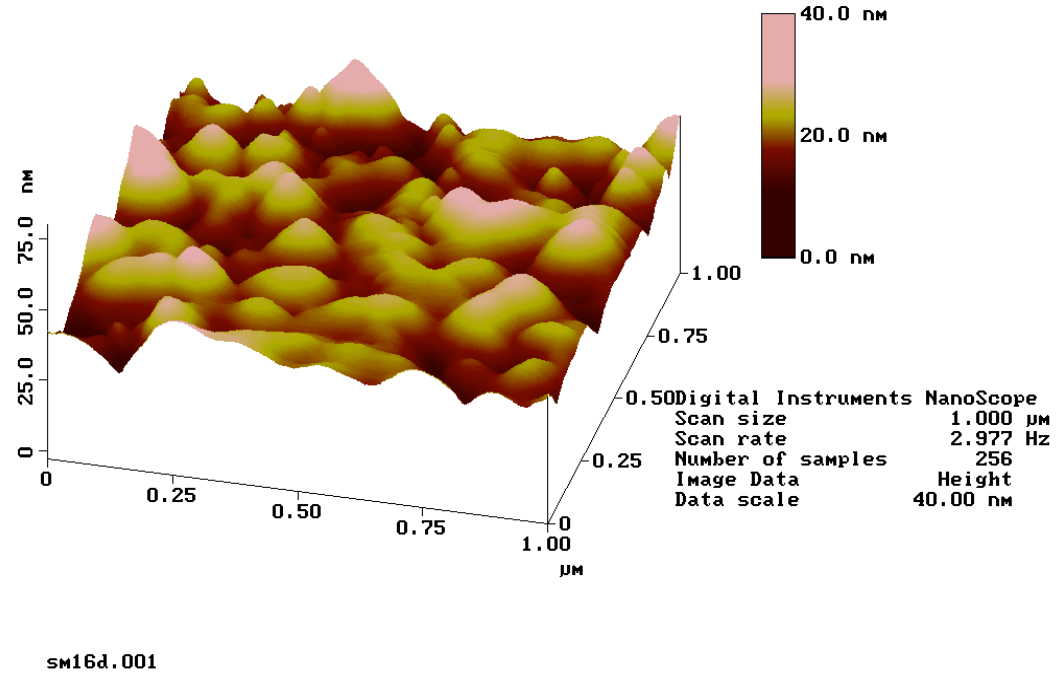

Figure 3.8 AFM image of $CuScO_2$ film after RTA. Rmax=30.5 nm, Rms=4.3 nm.

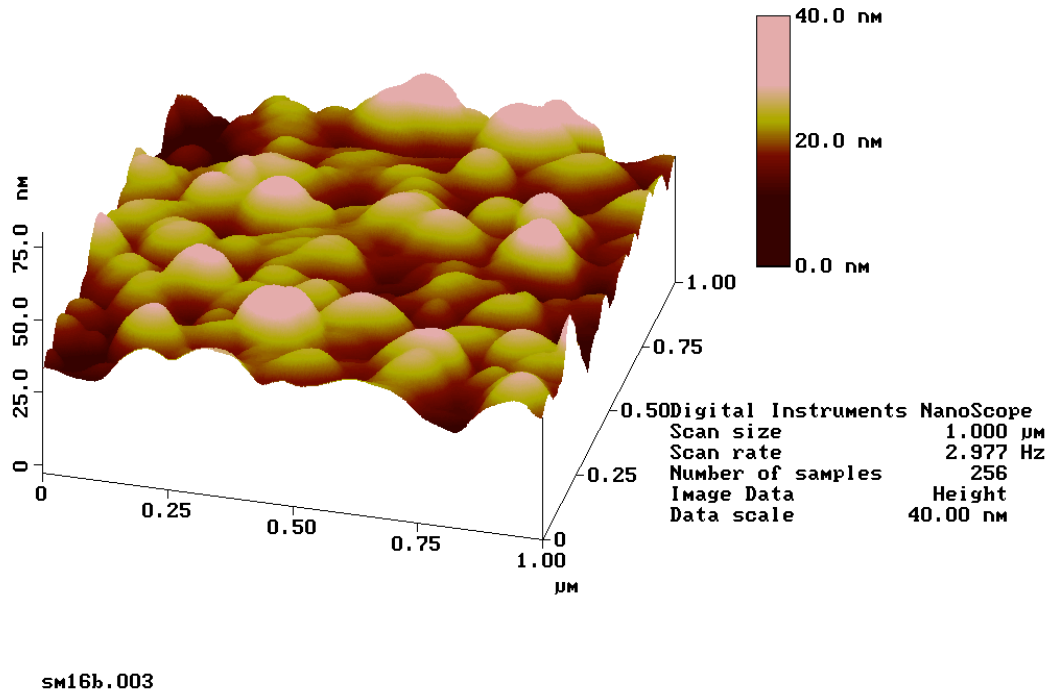

Figure 3.9 AFM image of oxygen intercalated $CuScO_2$ film. Rmax=35.1 nm, Rms=4.9 nm.

The as-deposited film in Fig. 3.7 is relatively smooth with small surface features and a maximum peak-to-valley height (Rmax) of 11.3 nm. The vertical scale bar is 15 nm. The roughness can be quantified by the root mean square roughness (Rms). This value is the standard deviation from the center of the mean plane (the average height of the surface). In the as-deposited film the Rms value is 1.6 nm. In the image of the film that has undergone the oxygen and argon RTA processing in Fig. 3.8, it can be seen that the surface features have increased in size significantly. As a comparison, the vertical scale is now 40 nm. The maximum peak-to-valley height is 30.5 nm and the Rms is 4.3 nm. Not only is there more height variation in the RTA'd films, but the features also appear larger in area. This proves that grain growth occurs during the annealing process. This supports the XRD data, which show an increase in

film crystallinity from the annealing process. These images can also be compared to that of the intercalated film in Fig. 3.9, also with a 40 nm scale. The maximum height variation is 35.1 nm and the Rms is 4.9 nm. The surface roughness did increase by a small amount compared to the RTA'd film, but this increase is not significant. The trend seen in the Rms and Rmax at various processing stages is summarized in Fig. 3.10.

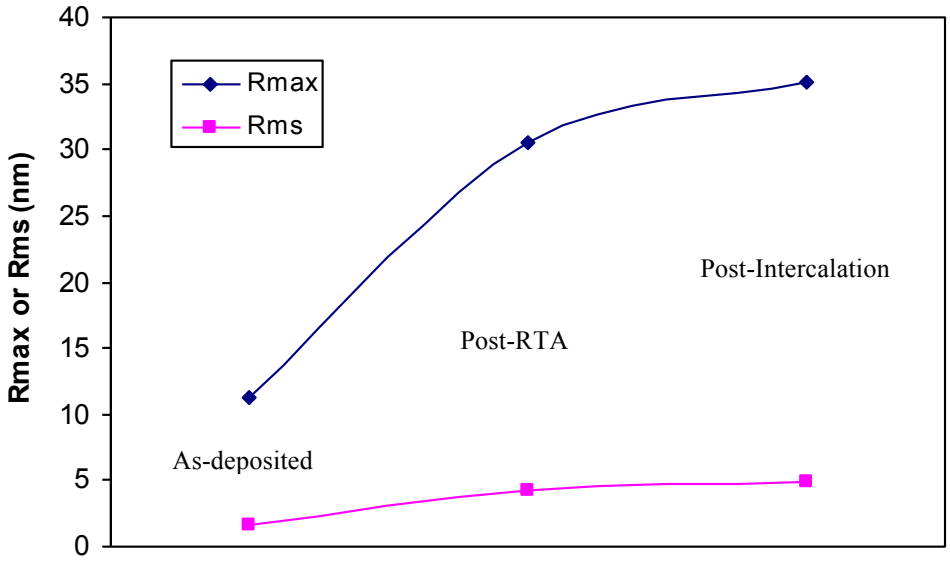

Figure 3.10 Maximum height (Rmax) and root mean square roughness (Rms) of as-deposited, post-RTA, and post-intercalation films.

There are some small changes in the crystal structure from the uptake of oxygen, most notably an expansion in the *a*-lattice constant as shown in the previous section; however, this does not have a significant effect on the surface. It is more likely that the slightly larger roughness is simply due to local variation across the film surface. This AFM analysis proves that the lower temperature at which the oxygen intercalation is done at (400^{o}C) is not a high enough temperature to incur any major changes in grain size.

3.2.3 Conclusion

AFM shows that there is a significant increase in surface roughness due to grain growth during the high temperature RTA. The intercalation does not incur any major changes in the surface morphology. About 10-15% of the total film thickness shows some variation in the surface morphology. This could present a problem if the material is to be used in a layered structure where another material would be deposited on top of it. A non-uniform interface between two materials in a semiconductor device could prove detrimental to its performance.

3.3 Electron Microprobe Analysis

3.3.1 Introduction

Electron microprobe analysis (EMPA) gives information about sample composition by analyzing the X-rays emitted as a result of high-energy electron bombardment. The several keV incident electrons excite core electrons in the sample to higher energy levels which subsequently lose their energy in the form of characteristic X-rays. In wavelength dispersive spectroscopy (WDS), these X-rays are diffracted at a certain angle by the lattice planes of different single crystals with known *d*-spacings and detected. From this information the wavelength of the characteristic X-rays is determined and the compositional elements identified. The atomic percent of the constituent elements can be found based on the relative intensities of the characteristic X-rays. This method is quantitative with proper

calibration, but gives information only about the relative amounts of the elements present, not the phases in which they exist. In this experiment a 10 μm 7 keV beam was used.

3.3.2 Results and Discussion

Table 2 gives the average composition of two sets of films made from the 5% Mg and 15% Mg doped targets. Compositions are given after each processing step. Atomic percents are averages from five scans performed on each film at different areas on the surface. The atomic percents are normalized to Sc because it gives reliable data. The *x* corresponds to the amount of Mg in the chemical formula, $CuSc_{1-x}Mg_xO_{2+y}$, and is the ratio Mg/(Sc+Mg).

The convention used for labeling films in this experiment are UD for undoped, MD for medium doping, or films made from the 5% Mg target, and HD for high doping, or films made from the 15% Mg target. 1 signifies an as-deposited film, 2 is after the 750°C O_2 rapid thermal anneal (RTA) in which the film forms the $Cu_2Sc_2O_5$ phase, 3 is after the O_2 and the 900°C Ar RTA in which the $CuScO_2$ phase is formed, and 4 is after the RTA steps and oxygen intercalation with the film remaining as $CuScO_2$.

5% Mg doped target		Cu	Sc	O	Mg	*x*
As deposited	A%	13.98	26.01	58.96	1.04	
MD4-1	Normalized	0.54	1	2.27	0.04	0.040
post O2 RTA	A%	14.13	25.77	59.56	0.52	
MD4-2	Normalized	0.55	1	2.31	0.02	0.020
post Ar RTA	A%	19.26	29.31	50.87	0.56	
MD4-3	Normalized	0.66	1	1.74	0.02	0.019
post interc	A%	17.25	28.63	53.66	0.47	
MD4-4	Normalized	0.60	1	1.87	0.02	0.016
15% Mg doped target						
As deposited	A%	17.03	19.44	60.29	3.24	
HD6-1	Normalized	0.88	1	3.10	0.17	0.143
post O2 RTA	A%	18.09	19.68	58.91	3.32	
HD6-2	Normalized	0.92	1	2.99	0.17	0.144
post Ar RTA	A%	24.41	21.98	52.54	1.07	
HD6-3	Normalized	1.11	1	2.39	0.05	0.046
post interc	A%	22.86	18.67	57.48	0.98	
HD6-4	Normalized	1.22	1	3.08	0.05	0.050

Table 2 EMPA results after each processing step for two sets of films made from the 5% Mg and the 15% Mg doped sputter targets. Atomic %'s are given along with the data normalized to Sc. x=Mg/(Sc+Mg). The atomic %'s are corrected for the SiO_2 contribution from the substrate.

The Mg contents of the as-deposited films are close to the Mg content in the original target material with 4% in the film made from the 5% target, and 14.3% in the film made from the 15% target. After the RTA treatment the Mg content drastically decreases. About $^2/_3$ of the Mg is lost during the high temperature RTA processing stage. The oxygen intercalation does not alter the Mg content, but the overall percentage should decrease since more oxygen is being incorporated into the film. The final processed films contain only 1.6% Mg for the film made from the 5% Mg target, and 5% Mg for the film made from the 15% Mg target. The trend is summarized in Fig. 3.11 that shows the Mg/Sc ratio after each processing step for two sets of films made from the 5% Mg and the 15% Mg targets. It is likely that Mg

segregates from the film during the RTA to form MgO or Mg metal. The amount of segregation is too small to be detected using XRD. However, the segregation is questionable because the Mg would still show up in EMPA whether or not it was incorporated in the $CuScO_2$. It's possible that the beam totally missed the areas where Mg is present, but this is not likely with a 10 μm beam size. The areas of segregation would have to be very widely spaced apart.

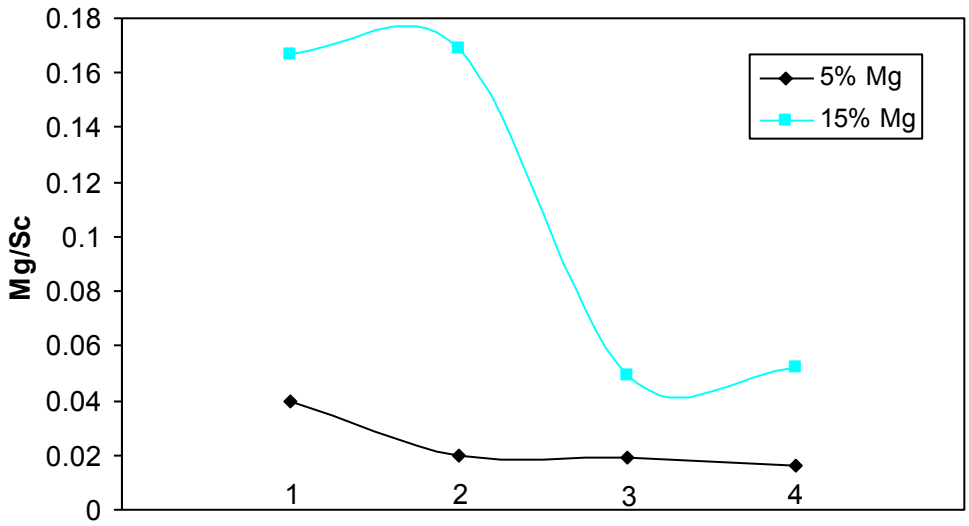

Figure 3.11 Mg/Sc ratio after each processing step for films made from the 5% and 15% Mg targets according to EMPA. 1 is as-deposited, 2 is after the O_2 RTA, 3 is after the O_2 and Ar RTA, and 4 is after intercalation.

The data in Table 2 shows the general trend of how the oxygen content changes after each processing step. The films become more oxygen-rich after the first RTA in oxygen. They are reduced from the argon RTA, and then the oxygen content is again increased from the intercalation. The changes after each processing step in the O/Sc ratio are summarized in Fig. 3.12 for both film sets. Both sets display similar behavior with the highly-doped film taking up slightly more oxygen.

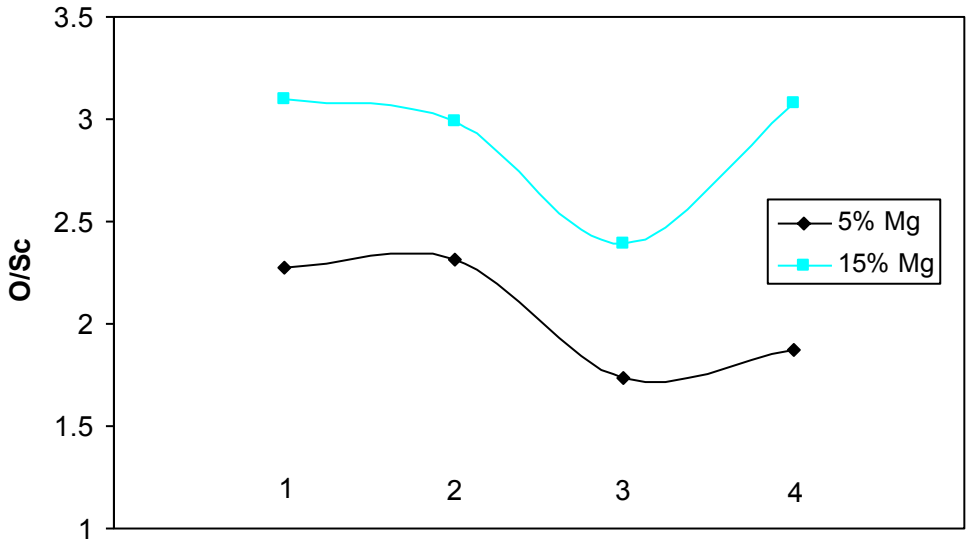

Figure 3.12 O/Sc ratio after each processing step for films made from the 5% and 15% Mg targets according to EMPA. 1 is as-deposited, 2 is after the O_2 RTA, 3 is after the Ar RTA, and 4 is after intercalation.

In research done at Oregon State University on the bulk powder form of this material it has been shown using thermo-gravimetric analysis that the maximum amount of oxygen that can be taken up corresponds to y=0.5 in $CuScO_{2+y}$ [26, 27]. It is shown in Fig. 3.12 that the O/Sc ratio varies from 1.9 for the intercalated film made from the 5% Mg target, to 3.1 for the intercalated film made from the 15% Mg target. Neither of these numbers is close to the optimal 2.5. There must surely be some error involved with the measurement. Also, the cation compositions do not appear to be stoichiometric. This conflicts with the XRD data in the previous chapter where it was shown that no strong impurity peaks are present.

The reasons for these conflicts are due to errors that arise in EMPA. First of all, not only does the electron beam interact with the film, but also the glass substrate beneath it. Thus EMPA also records substrate oxygen. To compensate, Si was

monitored and oxygen corresponding to the SiO_2 substrate was subtracted from the total atomic percent. Additionally, the teardrop-shaped excitation volume generated by the electron beam in the material has a different size and shape for different elements and compounds. So the oxygen that is in the SiO_2 substrate reacts differently with the beam than the oxygen in the film.

Problems also arise with the Cu analysis in EMPA when analyzing for Cu because the Cu Lα line is used, and it is difficult to know precisely what the absorption coefficient is for this line. Additionally, the Cu Lα and O Kα have large zones of excitation so there are problems with surface scattering and knowing precisely what the excitation volumes are [R. Nielsen, private commun.]. Earlier studies of YBaCuO showed consistent discrepancies between EPMA and Rutherford backscattering in the Cu:Y ratio [J. Tate, private commun.]. Sc, on the other hand is fairly reliable, and this is why the data was normalized to Sc. Mg, like Sc, gives more reliable data than O and Cu.

3.3.3 Conclusion

Although it is difficult to obtain information about film stoichiometry and oxygen content from the EMPA data, it was useful in this experiment to reveal roughly how much Mg is present in the films. It was shown that the final processed films contain approximately 1/3 of the Mg content of the original sputter targets, although it is not known whether the Mg segregates. The majority of the Mg is lost during the RTA processing. Precise quantitative analysis of the oxygen in the films using EMPA

analysis proves to be difficult, but qualitative information is available. It was shown how the various processing stages affect the amount of oxygen in the films.

3.4 Electrical Characterization

3.4.1 Introduction

Transport properties of films were characterized using three different techniques. Seebeck measurements were performed to verify the carrier type with all measured films displaying *p*-type behavior. Conductivity was measured at room temperature and as a function of temperature using two different configurations. The films display semiconductive behavior in that there is an increase in conductivity with increasing temperature due to thermal generation of carriers. The measured conductivities ranged from about $2x10^{-5}$ S/cm for undoped, non-intercalated films to $2x10^{1}$ S/cm for the heavily intercalated films. It was also attempted to measure the Hall mobility and carrier concentration via Hall measurements, but this technique proved unsuccessful due to the relatively high resistance of the films and the dc Hall voltage being too small to measure with the capability of the Hall setup.

3.4.2 Seebeck Measurements

In the Seebeck measurement, the sample was pressed against a pair of copper blocks, and one end of the sample was heated while the other end remained at room temperature. This causes carriers to diffuse from the hot end to the cooler end and the

resultant voltage is measured as the sample cools down and goes back to equilibrium. If the Seebeck coefficient, $S=\Delta V/\Delta T$, (the slope of the line fit to the data) is positive then the carriers are *p*-type, and if negative, they are *n*-type. The results for two intercalated $CuSc_{1-x}Mg_xO_{2+y}$ films are displayed in Fig. 3.13. Both films have a Seebeck coefficient of about +20 μV/K, verifying that the films are *p*-type. These measurements agree with previous results from measurements done on other $CuScO_2$ films by Robert Kykyneshi, Dara Easely, and others at Oregon State University so it was not necessary to measure additional films.

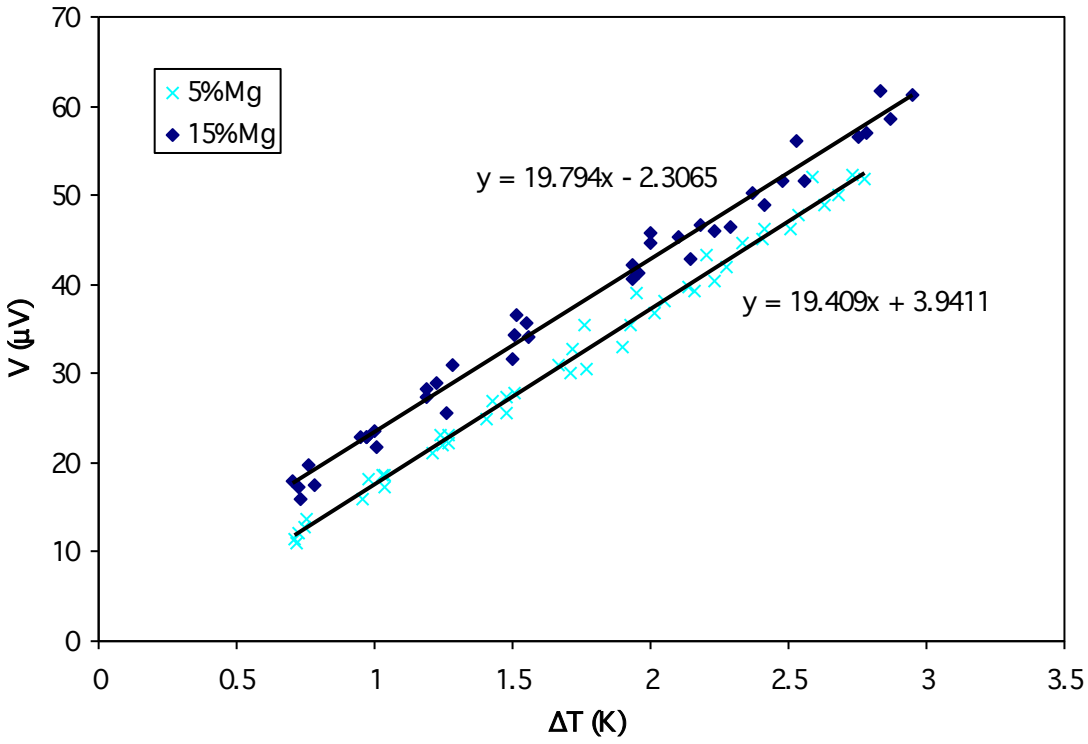

Figure 3.13 Seebeck measurements on two intercalated $CuSc_{1-x}Mg_xO_{2+y}$ films made from the 5% Mg and the 15% Mg targets. For both films the Seebeck coefficient, given by the slope of the line fit, is about +20 μV/K.

3.4.3 Conductivity

Conductivity was measured at room temperature and as a function of temperature using a co-linear 4-point probe. The geometry of the setup is depicted in Fig. 3.14 (A). A current is passed through the two outer probes, and the resultant voltage is measured between the two inner probes with all probes being equally spaced apart. Having 4 probes eliminates the contact resistance inherent in 2 probe measurements. To check for reproducibility, room temperature conductivities were also measured using a Van der Pauw setup. A Van der Pauw configuration is also a 4-point probe technique, but instead of being linear, the probes are placed on the four corners of the film, forming a square as depicted in Fig. 3.14 (B). The current path is between any two of the probes, and it is switched between all the probes while the voltage is measured at opposing probes.

In both configurations, Ohmic behavior was observed so it was not necessary to use metallic contacts between the film and the probes. The resistivity was determined from the measured resistance using the thin film approximation formula, $\rho=\pi Rt/ln\ 2$, where R is the measured resistance and t is the film thickness [29]. This approximation can be used when the film thickness is much less than the distance between the probes. To account for variability in measurements, several measurements were performed on each film and an average resistivity was taken.

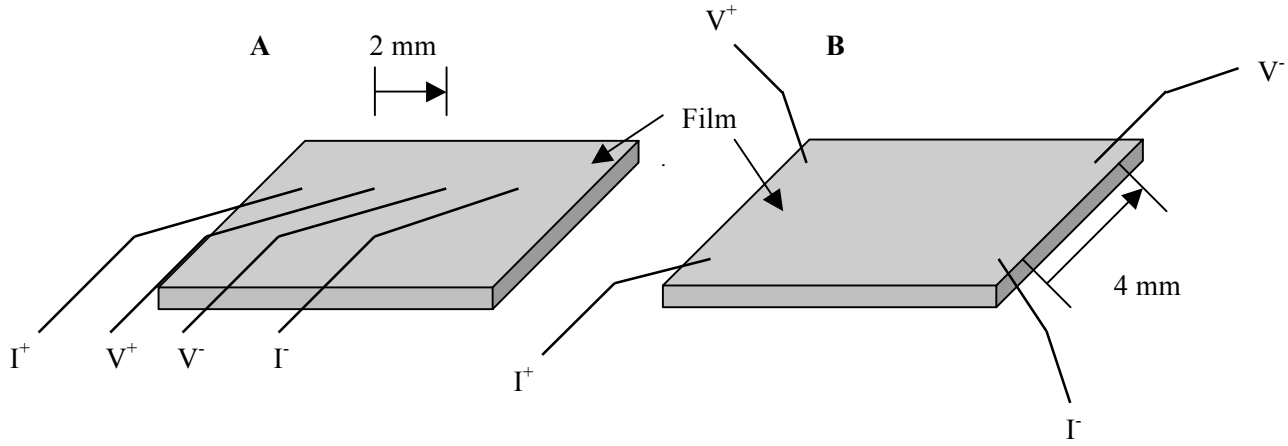

Figure 3.14 Geometry of (A) Co-linear and (B) Van der Pauw setups used to measure conductivity of films. The distance between probes is 2 mm in (A), and 4 mm in (B).

Temperature-dependent conductivity measurements were performed on several films. In this setup, the co-linear configuration is used at the end of a probe that is inserted into a cryostat. The sample is cooled to ~80 K using liquid nitrogen and is allowed to slowly warm back up to room temperature as the liquid nitrogen evaporates. The conductivity of a semiconductor increases with increasing temperature because carriers are being thermally generated, whereas the conductivity of a metal decreases with increasing temperature due to scattering by phonons. These $CuSc_{1-x}Mg_xO_{2+y}$ films display semiconductive behavior, but decreasingly for more conductive films. Fig. 3.15 displays the conductivity as a function of inverse temperature of two intercalated films made from the undoped and 5% Mg doped sputter targets. Both films display roughly the same temperature behavior with the doped film being about twice as conductive as the undoped film.

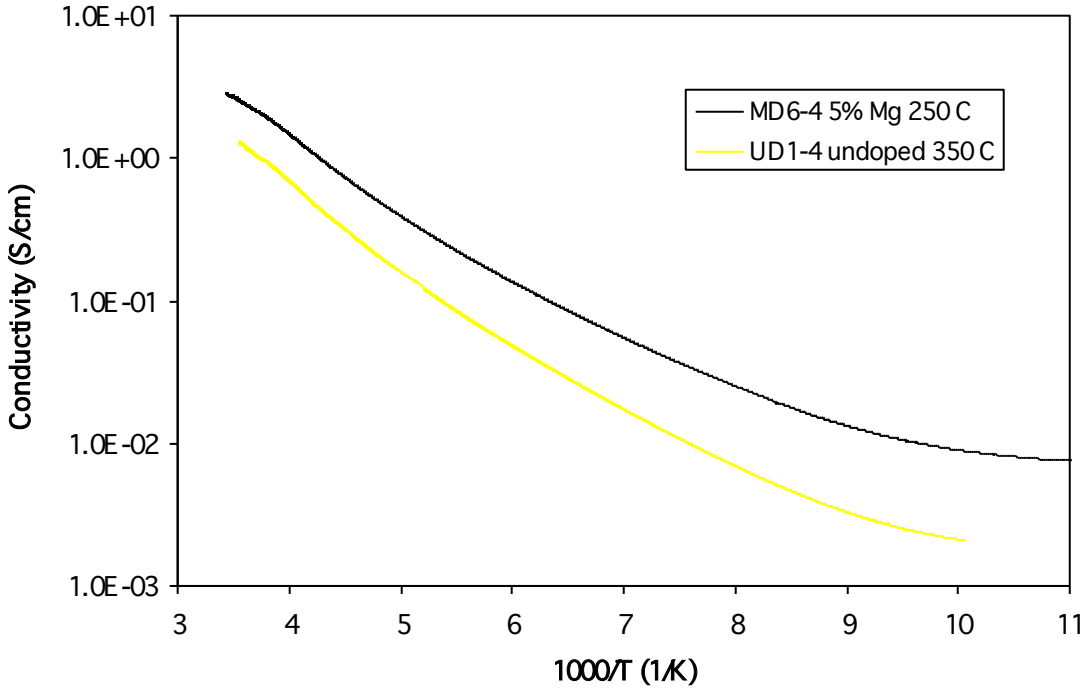

Figure 3.15 Conductivity vs. *1/T* for two intercalated $CuSc_{1-x}Mg_xO_2$ films.

Fig. 3.16 displays the conductivity as a function of $1/T^{1/4}$ for the same two films in Fig. 3.15. These two dependencies of conductivity on two different powers of inverse temperature follow different models of carrier transport in semiconductors. The carriers move through the material by hopping via two different mechanisms: Thermally activated hopping and variable range hopping [30]. In thermally activated hopping, the electron (or hole) must acquire energy from a phonon each time it moves from one adjacent localized state to another. Variable range is different from the thermally activated process in that the hopping is not necessarily to an adjacent site, but "hops" to more distant sites are also possible via tunneling. The variable range mechanism is generally effective at lower temperatures [31].

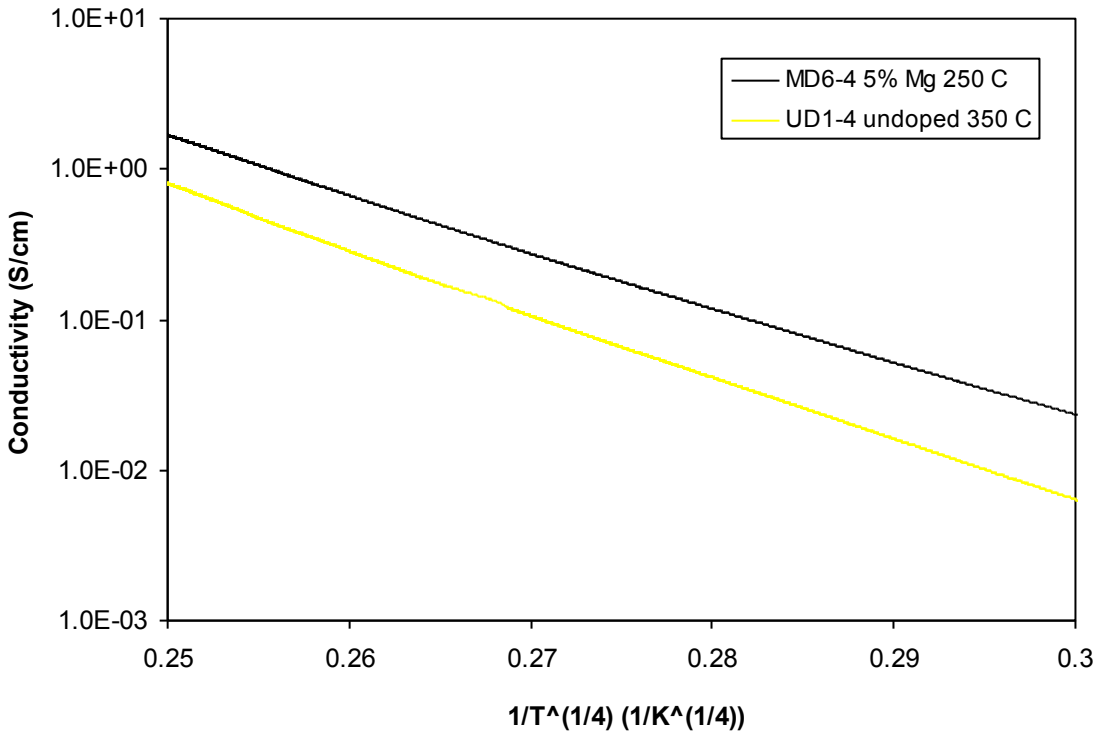

Figure 3.16 Conductivity vs. $1/T^{1/4}$ for two intercalated $CuSc_{1-x}Mg_xO_2$ films. Since $ln\ \sigma$ is linear with $1/T^{1/4}$, it is likely that variable range rather than thermally activated hopping is the dominant transport mechanism.

In most delafossites, such as $CuAlO_2$, variable range hopping between states on adjacent Cu sites is effective at lower temperatures below about 220 K, whereas the thermally activated carriers become more dominant at higher temperatures [19]. Thermally activated behavior is modeled by $\sigma/\sigma_o=exp[-E_a/kT]$ where σ is the conductivity, σ_o is the conductivity at infinite temperature, E_a is the activation energy, k is Bolztmann's constant, and T is the temperature [30]. E_a is determined by fitting a straight line to a plot of $ln\ \sigma$ vs. $1/T$ as in Fig. 3.15. For these films E_a is about 100 meV. This value is in similar to the calculated activation energies of 95 meV and 110 meV found by others in research on this material [14, 16]. It is seen in Fig. 3.16 that the $ln\ \sigma$ data more closely follows a linear behavior with $1/T^{1/4}$. This behavior is

modeled by $\sigma/\sigma_o=exp[-(T_o/T)^{1/4}]$, where the temperature parameter, T_o, is simply the slope of the graph of ln σ vs. $1/T^{1/4}$. The data is consistent with variable range hopping [30] and is dominant over a wide temperature range. Other research also points to this conclusion [17].

3.4.4 Effects of Magnesium Doping and Oxygen Intercalation on Conductivity

In order to best determine the effect of the Mg doping, the room temperature conductivity (~295 K) was measured for annealed, non-intercalated films. In the non-intercalated films, the $CuScO_2$ phase has fully formed, but there is no excess oxygen so the conductivity can be entirely attributed to the Mg doping and intrinsic defects. Room temperature conductivities were measured using the same 4-point probe used for the temperature-dependent measurements without inserting it in the cryostat. A Van der Pauw configuration on a different system was also used with the only difference found between the two configurations within reasonable error.

Fig. 3.17 shows the room temperature conductivities of the annealed, non-intercalated films as a function of Mg doping. Films from each of the undoped, 5% Mg doped, and 15% Mg doped sputter targets were compared. According to the EMPA results discussed in a previous chapter, the Mg contents are actually about 0%, 1.6%, and 5% for films made from the 0%, 5% and 15% sputter targets, respectively. For reasons of consistency and accuracy the % Mg in the sputter targets is referred to instead of the actual doping level. The non-intercalated films are highly resistive and proved difficult to measure, especially the undoped films since the currents used were as small as several hundred picoamps and this led to current leakage. Films were

sputtered onto glass substrates that were held at different temperatures. In order to observe the effect of substrate temperature, a comparison was made between films deposited at 150°C, 250°C, and 350°C.

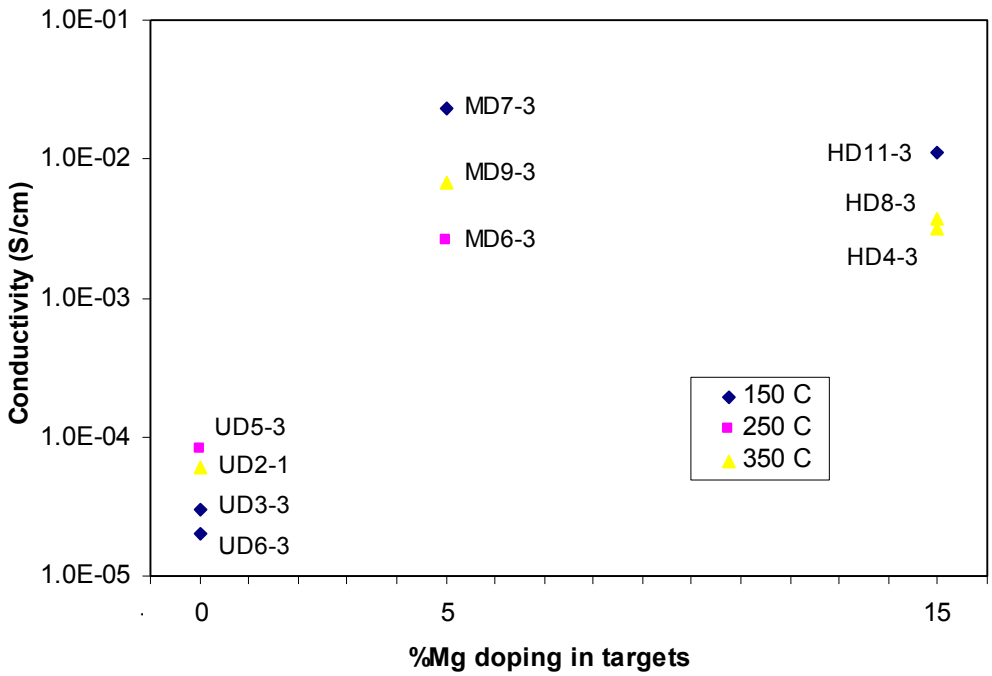

Figure 3.17 Room temperature conductivities (4-pt) of annealed, non-intercalated $CuSc_{1-x}Mg_xO_2$ films as a function of Mg doping in the sputter targets for three different substrate temperatures.

The conductivities of the doped films are 2-3 orders of magnitude larger than the undoped films. In the most conductive film (MD7-3), σ=2.3x10^{-2} S/cm. This is three orders of magnitude higher than the value of the least conductive film (UD6-3), σ=2x10^{-5}. This proves the Mg is effective as a dopant by improving conductivity, however, the conductivity is still substantially low for a semiconductor. It is possible that the hole contributed by the Mg is localized and thus can only make a limited contribution to the conductivity. It is has been proposed that either the hole must

migrate from the Mg site to the Cu planes in order to become an active carrier, or the conduction path changes to the more difficult Cu-O-Mg-O-Cu [26]. With doping via oxygen intercalation, on the other hand, the holes are created near the Cu sites, which may make them better able to contribute to conductivity.

Interestingly, the films made from the 5% Mg sputter target are about twice as conductive as the films made from the 15% Mg target, however this difference is within the limits of reproducibility seen with these films. A reason for the films made from the 15% Mg target being slightly less conducting could be either because the extra carriers are not incorporated and the Mg impurities cause scattering, or because they are incorporated but their effect is counteracted by ionized impurity scattering.

A trend is also noticed between different substrate temperatures in Fig. 3.17. For the films made from the Mg doped targets, the depositions at 150^{o}C produced more conducting films than the ones made at 350^{o}C. The effect of substrate temperature in the Mg doped films is not seen as clearly in the undoped films, with the films deposited at 150^{o}C being the least conductive, and the film deposited at 250^{o}C being the most conductive. The reason for the increased conductivity at lower substrate temperatures is not completely understood. Films deposited at higher substrate temperatures are generally more crystalline. Usually a higher quality, more highly crystalline material is less resistive than the amorphous version due to scattering of carriers off grain boundaries and other defects. So it would be expected to see the opposite trend of what is seen in the data. Further, the films do undergo the same high temperature annealing process at 750^{o}C and 900^{o}C so this could overrule any slight variations in as-deposited crystallinity.

It is also possible that the films have a higher Mg content at lower temperatures if Mg is more easily incorporated into the growing film. Yet another possibility would be that excess oxygen is being incorporated at higher levels at lower substrate temperatures. This is supported by research in ZnO:Al [32] and ITO [33] in which the excess oxygen content at lower substrate temperatures reduces conductivity (oxygen vacancies *increase* conductivity in these *n*-type materials). But this example seems least likely, as once again, the high temperature RTA process should overrule this effect because there should not be any excess oxygen in the films after the Ar reduction.

Intercalated films are substantially more conductive than the non-intercalated ones. In previous research it was shown that the conductivity in fully intercalated films approaches 30 S/cm [16], 3 orders of magnitude higher than the most conductive non-intercalated films. In order to directly compare Mg doping in intercalated films it was necessary to intercalate all the films together because the conductivity is very sensitive to the oxygen intercalation. Even if identical parameters were used, there was some variability in the system that made it difficult to quantitatively compare films that were not intercalated together.

No long-term loss of intercalated oxygen was observed. Films measured weeks or even months after being intercalated displayed the same conductivity as they did immediately after intercalation.

Fig. 3.18 shows room temperature conductivities in intercalated films as a function of Mg doping for two different substrate temperatures of 150^{o}C and 350^{o}C. The films were intercalated together in 400^{+}/-10 Torr oxygen at 400^{o}C for 9 hours.

These conditions lead to an intermediate amount of intercalated excess oxygen so that the films are almost, but not quite fully intercalated. Fig. 3.17 shows that unlike the non-intercalated films, the most conductive films are the highly doped ones. It has been proposed that the Mg doping increases uptake of oxygen during intercalation [34]. As in the case of the non-intercalated films, there is an effect of the substrate temperature on the conductivity. Again, all the films deposited at 150°C are more conducting than the films deposited at 350°C with the largest difference between the two undoped films, and the smallest difference between the two highly doped films.

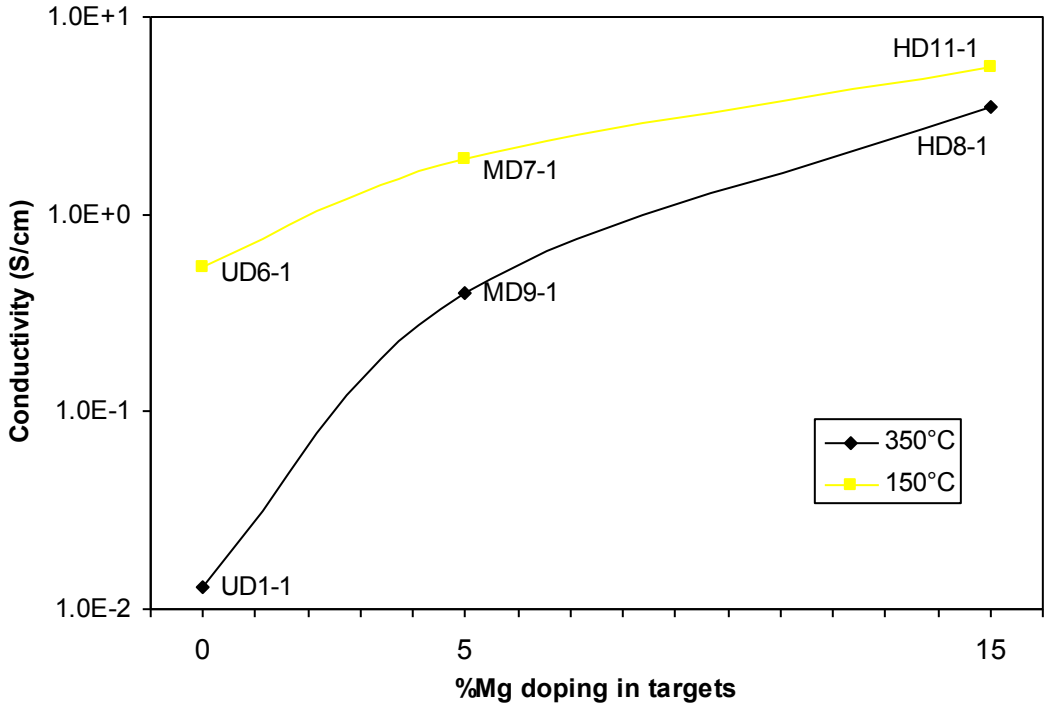

Figure 3.18 Room temperature conductivity (4-pt) for intercalated $CuSc_{1-x}Mg_xO_{2+y}$ films as a function of %Mg in the sputter targets.

It is possible to further increase the conductivity in $CuScO_2$ films by increasing the time of intercalation and pressure of oxygen. The temperature cannot be

increased significantly beyond 400°C because of a decomposition that takes place around 450°C [26, 27]. Additionally, if the films are heated past ~600°C in an oxygen atmosphere the $Cu_2Sc_2O_5$ phase forms. In order to observe the maximum amount of conductivity that can be imparted in $CuScO_2$ films due to oxygen intercalation, films were intercalated at high pressures for an extended period of time. The films were intercalated at 400°C in 800 p.s.i. O_2 for 24 hours. The results are displayed in Fig. 3.19.

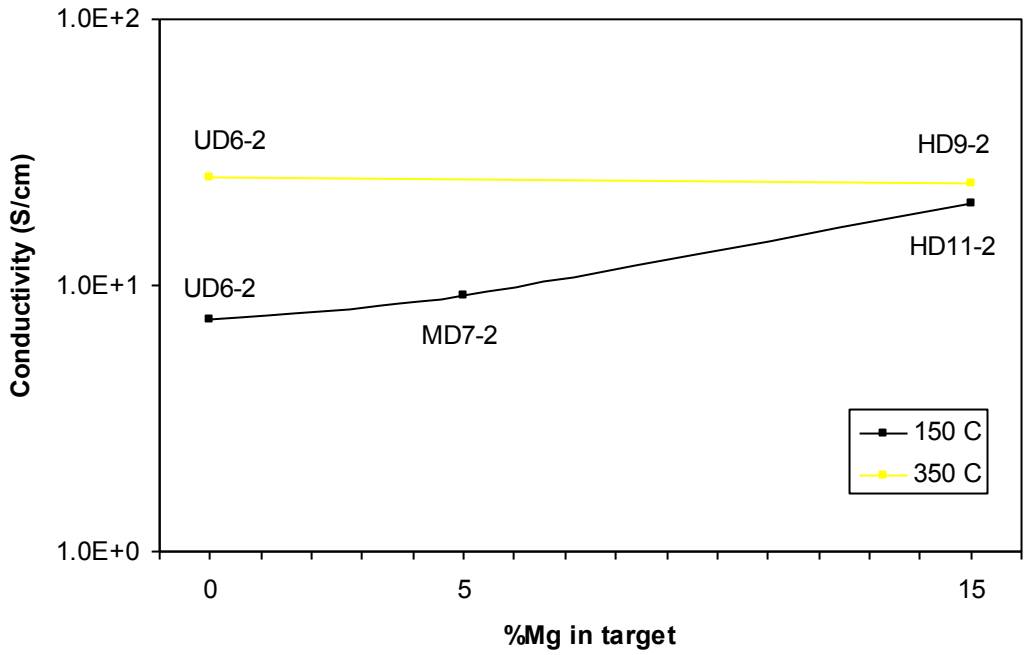

Figure 3.19 Room temperature conductivities (4-pt) of fully-intercalated $CuSc_{1-x}Mg_xO_2$ films made from sputter targets with different Mg doping. Films were deposited at 150°C and 350°C substrate temperatures.

The maximum conductivity observed was 26 S/cm in the undoped film deposited as 350°C (UD6-2). The effect of Mg doping is not as evident as it is in the non-intercalated films and the films intercalated at lower oxygen pressure. The films deposited at 150°C do display a dependence on Mg doping with the highly doped film

(20 S/cm) being 2.5 times more conductive than the undoped film (8 S/cm). But this dependence is not as strong as in the non-intercalated and low pressure intercalated films. For the films deposited at 350°C the undoped film (26 S/cm) has a similar conductivity to the highly doped film (24 S/cm). Saturating the films with oxygen appears to effectively wash out the effect of the Mg dopant. The conductivity is dominated by the oxygen intercalation. Reliable data was not obtained for a film made from the 5% Mg target deposited at 350°C due to inhomogeneous films.

3.4.5 Conclusion

To summarize the measured electrical properties, Seebeck measurements verified that the films display *p*-type behavior with a Seebeck coefficient of +20 V/K. The conductivity in $CuScO_2$ can be modulated by six orders of magnitude from about 10^{-5} to 10^{1} S/cm by varying the Mg doping and oxygen intercalation conditions. It was found that the Mg doping improves conductivity by up to three orders of magnitude from $2x10^{-5}$ S/cm to $3x10^{-2}$ S/cm. Oxygen intercalation improves conductivity by an additional three orders of magnitude up to about $2x10^{1}$ S/cm. In the fully intercalated films the effect of the Mg doping is effectively washed out; the fully intercalated undoped films are as conductive as the highly doped films. Additionally, the effect of substrate temperature was also observed with films deposited at 150°C generally more conductive than films deposited at 350°C in the non-intercalated and the films intercalated at lower oxygen pressure. The opposite effect of substrate temperature was observed in the films intercalated at high oxygen pressure. The maximum

observed conductivity was 26 S/cm. This is close to the previously reported maximum conductivity of 30 S/cm [16].

3.5 Optical Characterization

3.5.1 Introduction

The optical properties of $CuSc_{1-x}Mg_xO_{2+y}$ films at final and intermediate processing stages were measured using a UV-visible spectrometer. With this technique, a monochromatic beam of light is incident on a film and the intensity of the transmitted and reflected light is measured. From this information the absorption coefficient can be determined, and thus an estimate of the optical band gap can be made.

The transmission and reflection were measured in the ultraviolet to near-infrared range with incident light of wavelength 225 to 900 nm using a Xe light source and a double monochromator. Lenses and mirrors were used to focus the beam on the sample, and the transmitted or reflected beam was measured with a silicon photodetector attached to an optical power meter and interfaced with a computer for data acquisition. A detailed description of the system can be found in the senior thesis of Levi Kilcher [35].

3.5.2 Optical Characterization of Films After Each Processing Step

Fig. 3.20 shows the transmission (*T*), reflection (*R*), and *T/(1-R)* for an undoped, annealed, non-intercalated 100 nm thick film on a 1 mm thick amorphous silica substrate. The average transmission of this film in the visible region of the spectrum (400-700 nm) is about 70%. This value is about 90% for an ITO film of equivalent thickness. The effects of the lamp were accounted for by dividing the raw transmission and reflection intensities by the direct lamp spectrum. The *T/(1-R)* analysis removes the interference fringes caused by internal reflection and is used to calculate the absorption coefficient, α, according to $T/(1-R) = I_t / I_o = e^{-\alpha \cdot t}$, where I_t is the transmitted intensity, I_o is the incident intensity, and t is the film thickness [35, 49].

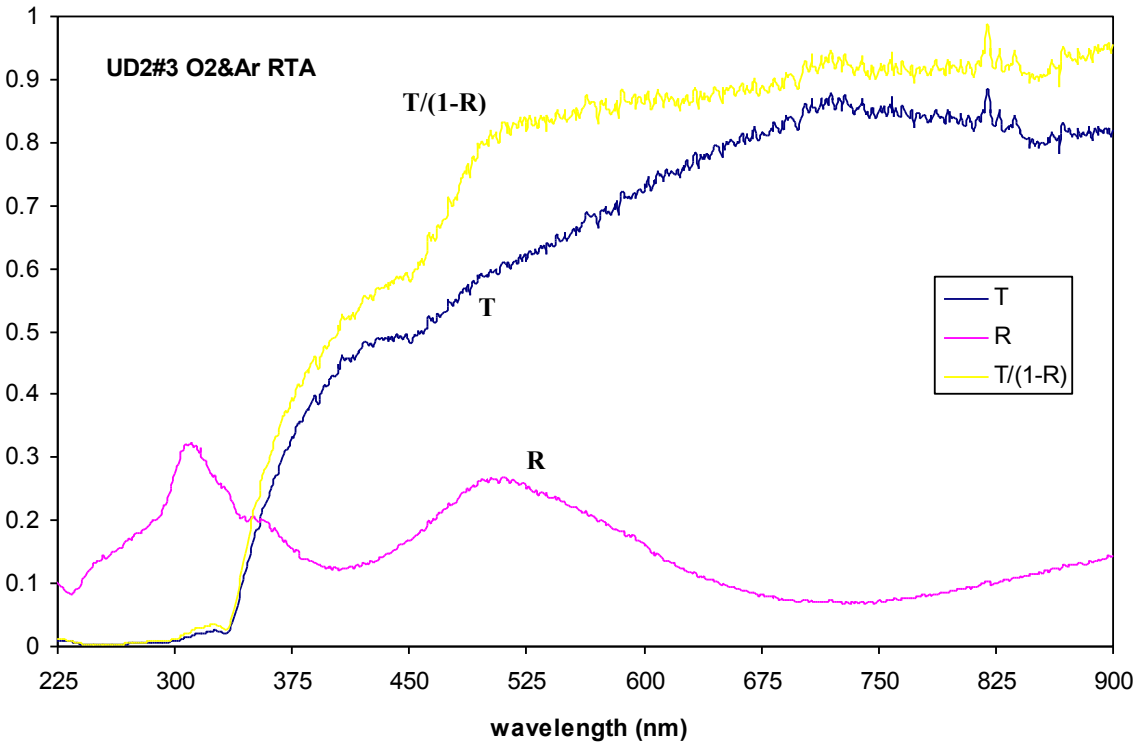

Figure 3.20 Transmission (*T*), reflection (*R*), and *T/(1-R)* in the UV to near-IR range for a 100 nm thick annealed, non-intercalated $CuScO_2$ film.

The average value of *T/(1-R)* in the visible region is about 85%, as seen in Fig. 3.20. This translates to an absorption coefficient of about $2x10^4$ cm^{-1}. Photon energy, *E*, relates to the wavelength, λ, inversely according to $E=hc/\lambda \approx 1240$ nm·eV/λ. The film is very transparent at wavelengths greater than 500 nm. The substrate reflects about 6% of light in the visible region with no absorption. It appears in the *T/(1-R)* curve that there are two absorption mechanisms in effect because at about 450 nm there is a change of slope. Virtually all of the high energy photons in the UV part (< 340 nm) of the spectrum are absorbed by the material, as evidenced by the fraction transmitted being close to zero along and the reflection around 15%. The peak in the reflection is anomalous and is not seen in other transparent oxides such as ITO, ZnO, $MgSnO_3$, Zn_2SnO_3, or any other of the *p*-type sulfides like BaCuSF or its variants.

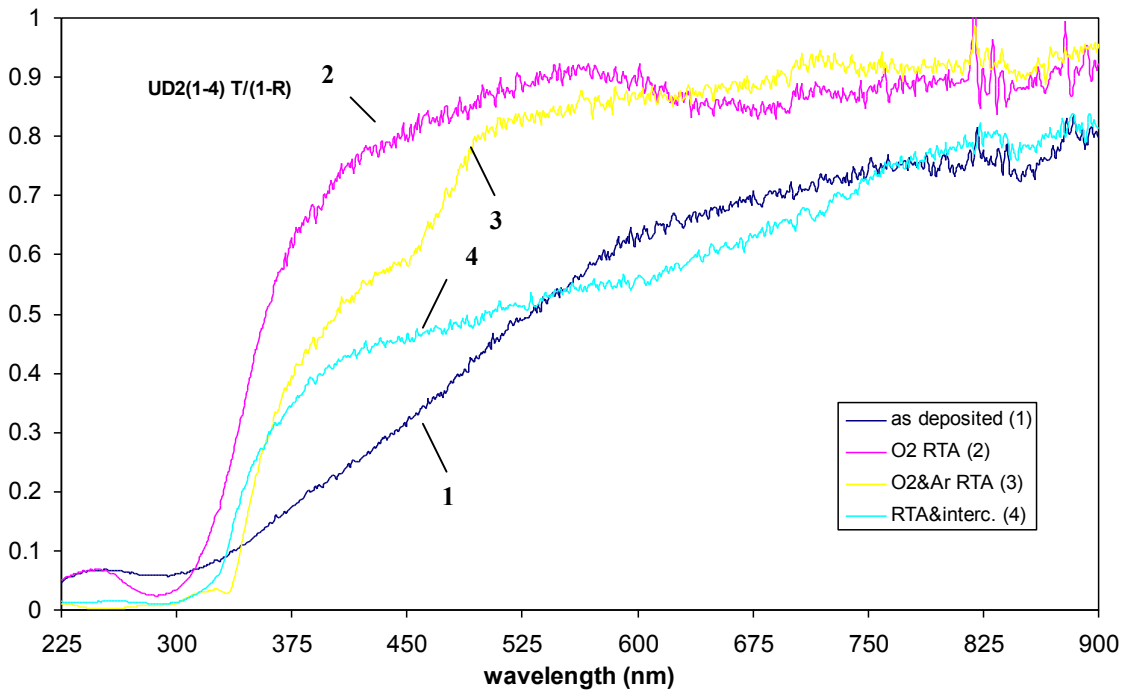

Figure 3.21 *T/(1-R)*=$e^{-\alpha \cdot t}$ after each of the four processing steps for 100 nm thick $CuScO_2$ films: (1) as-deposited, (2) after the O_2 RTA, (3) after the Ar RTA, and (4) RTA & intercalated.

In Fig. 3.21, *T/(1-R)* is shown for 100 nm thick films after each processing step. Film 1 is as-deposited, film 2 is after the 750°C O_2 RTA, film 3 is after both the O_2 and the 900°C Ar RTA, and film 4 has been annealed and intercalated at 400°C for 9 hrs. in 400 Torr oxygen. Film 3 is the same one shown in Fig. 3.20.

The as deposited film (1) transmits the least amount of light through the visible spectrum and is thus the darkest of the four films. Film 2 transmits all the way through the visible part of the spectrum up to about 400 nm (3.1 eV). This means that the $Cu_2Sc_2O_5$ phase has a larger band gap than the $CuScO_2$ phases, which offers an explanation as to the difficulty of making it conductive. Film 3 is similar to film 2 at wavelengths longer than about 500 nm, however, the absorption edge takes place at a lower energy. This corresponds to the band gap being somewhat smaller. The transmission of film 4 is significantly reduced from the intercalation treatment. The average transmission through the visible portion of the spectrum is about 50%. The intercalation process evidently introduces defect states in the gap that contribute to absorption across the spectrum.

In Fig. 3.22, the absorption coefficient, α, determined as discussed earlier, is plotted as a function of photon energy for the same set of 100 nm thick $CuScO_2$ films. The as-deposited film (1) has the highest absorption of visible light (2-3.1 eV), and the lowest absorption at energies higher than the visible. It also has the least structure with no clearly defined absorption edge. The annealed films (2,3) have a more developed energy gap and are more transparent at visible energies. Film 3 has the highest absorption in the UV ($>$ 4eV). The intercalated film (4) has some of the same structure as the O_2 and Ar RTA'd film, but it absorbs more visible light. The

average absorption coefficients in the visible region are $8.0x10^4$ cm^{-1} for (1), $1.5x10^4$ cm^{-1} for (2), $2.0x10^4$ cm^{-1} for (3), and $7.5x10^4$ cm^{-1} for (4). The high pressure intercalation at $4x10^4$ Torr resulted in a film with an absorption coefficient of $1.5x10^5$ cm^{-1}, twice that of the film intercalated at low oxygen pressure. *T/(1-R)* in the visible for this film was about 30%.

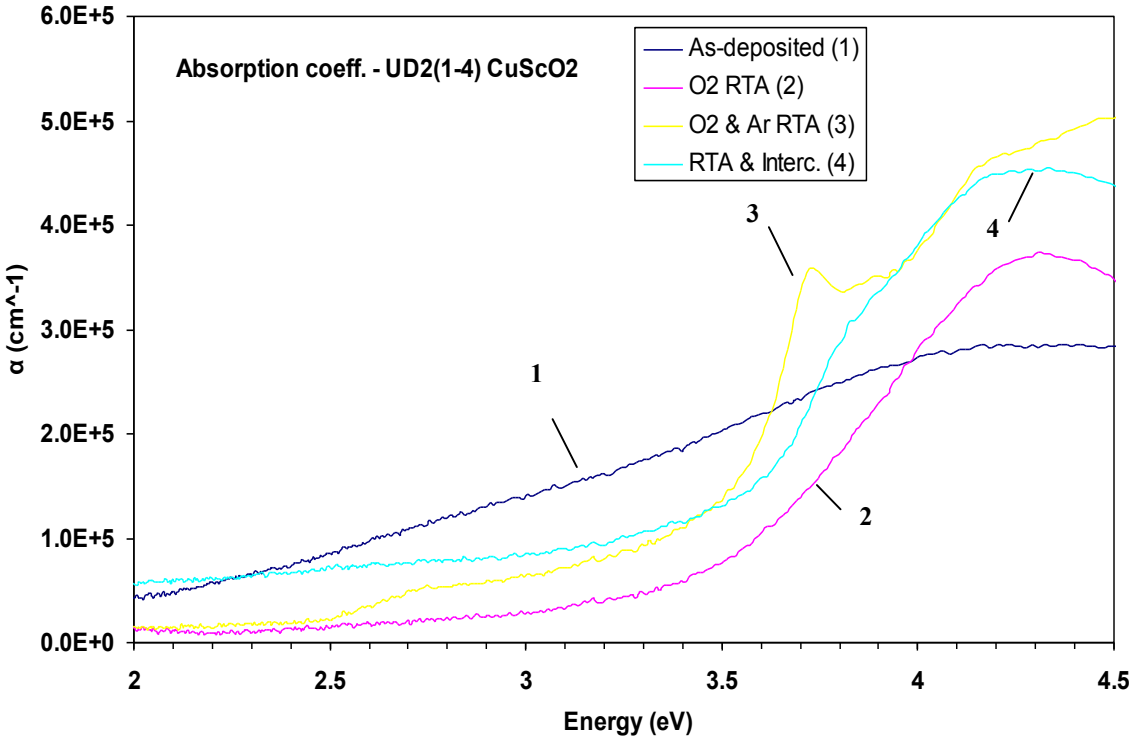

Figure 3.22 α vs. E for 100 nm $CuScO_2$ films:
(1) as-deposited, (2) O_2 RTA, (3) O_2 & Ar RTA, (4) RTA & intercalated.

3.5.3 Band Gap Analysis

In order to obtain values for the band gap, $(\alpha E)^2$ is plotted *vs.* E for a direct band gap, and $(\alpha E)^{1/2}$ is plotted *vs.* E for an indirect band gap, where α is the energy dependent absorption coefficient, and E is the photon energy, $h\upsilon$ [35, 50]. $(\alpha E)^2$ is plotted for the same film set as in the previous plots in Fig. 3.23. The band gap is

determined by drawing a straight line along the absorption edge and taking the value of the intercept of this line with the energy axis. This value was 3.6 eV for a direct band gap in the intercalated film. A value for the indirect band gap could also be determined using $(\alpha E)^{1/2}$ *vs. E*. There is some evidence for such a gap near 2 eV, but it is far from conclusive. There has been evidence using spectroscopy of an indirect band gap in $CuAlO_2$ [19]. Band structure calculations of delafossite materials show

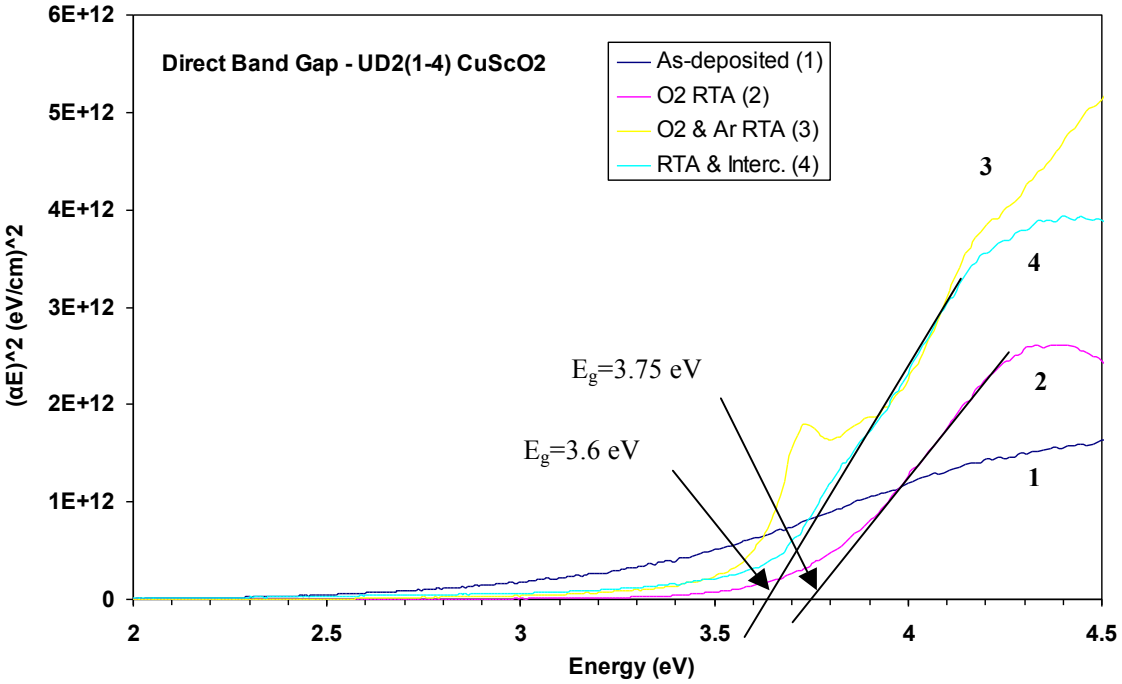

Figure 3.23 Plot of $(\alpha E)^2$ vs. *E* for the direct band gaps of 100 nm $CuScO_2$ films. (1) as-deposited, (2) O_2 RTA, (3) O_2 & Ar RTA, and (4) RTA & intercalated. The estimated direct band gap in the intercalated film is 3.6 eV.

an indirect band gap at energies lower than the direct band gap [37], however it has been suggested that the indirect transition is suppressed and is thus not favorable [38].

Film 3 shows the same absorption edge as in film 4, but a persistent feature is the lower energy absorption in film 3 that is absent in film 4. This absorption occurs at about 3.57 eV; slightly less than the band gap determined in the intercalated film.

This feature is thought to be excitonic. The band gap of the $Cu_2Sc_2O_5$ phase (film 2) is higher in energy than the $CuScO_2$ phase (films 3 and 4) and was determined to be about 3.75 eV. The as-deposited film shows no distinct absorption edge so a band gap cannot be determined for it.

3.5.4 Effect of Mg Doping on Optical Properties

It has been shown that oxygen intercalation decreases the transparency of films by increasing absorption over the entire visible range. The effect of the Mg doping on the transparency is shown in Figs. 3.24 and 3.25. These are plots of *T/(1-R)* and the absorption coefficient, α, for two annealed, non-intercalated films, one undoped and one made from the 15% Mg target with conductivities of $6x10^{-5}$ S/cm and $3.7x10^{-3}$ S/cm, respectively. To the naked eye the films look almost identical and are very transparent with a faint pink-blue shade. The measured *T/(1-R)* in the films is very similar with values of about 85-90% in the visible spectrum. To account for differences in film thickness (100 nm for the undoped film and 190 nm for the doped film), α is shown in Fig. 3.25 as a function of energy. The absorption of both films is very similar with the undoped film being just slightly more absorbing over most of the spectrum from about 2.7 to 4.5 eV, but this difference could be caused by error in the thickness measurement since absorption varies exponentially with thickness. Both films display an average value of α in the visible range of about $2x10^4$ cm^{-1}.

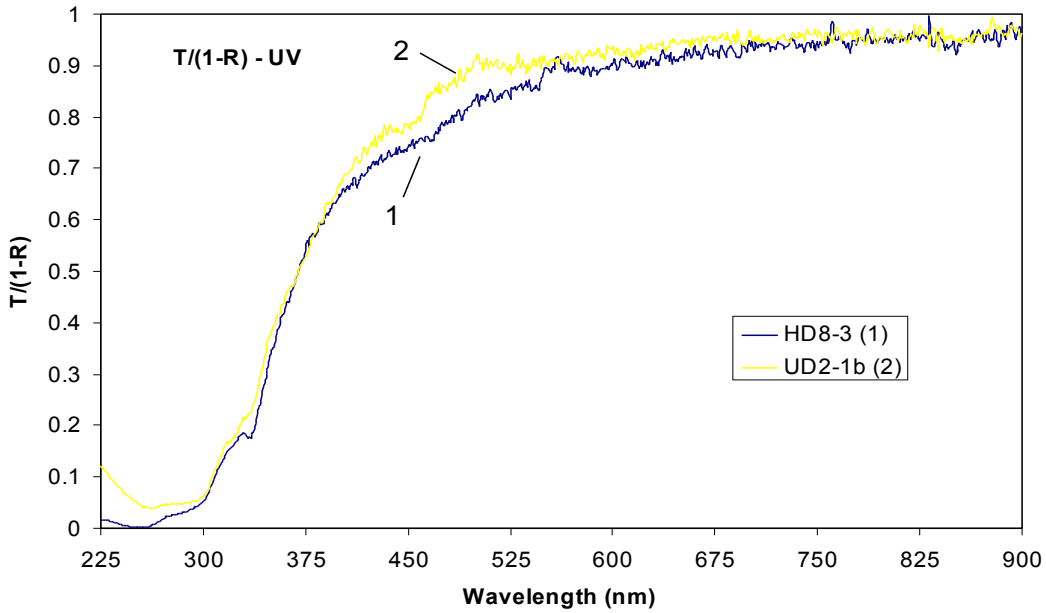

Figure 3.24 *T/(1-R) vs*. wavelength of incident light for two annealed, non-intercalated $CuSc_{1-x}Mg_xO_2$ films made from the 15% Mg doped (1) and undoped (2) sputter targets. The thickness is 100 nm for the undoped film and 190 nm for the doped film.

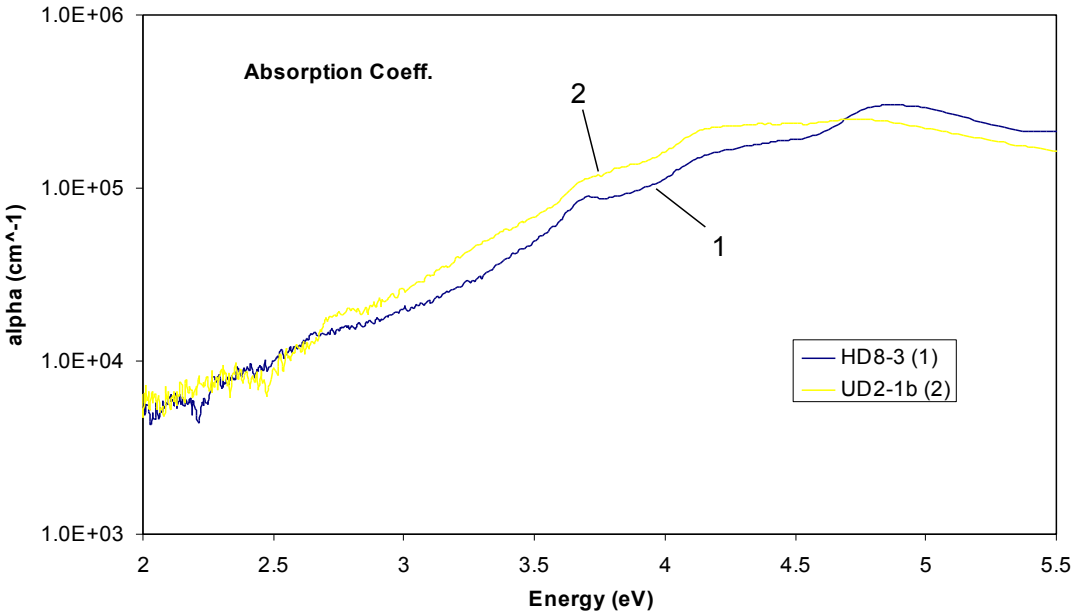

Figure 3.25 log α *vs*. energy for two annealed, non-intercalated $CuSc_{1-x}Mg_xO_2$ films made from the 15% Mg doped (1) and undoped (2) sputter targets.

3.5.5 Conclusion

Optical analysis was used to assess the transmission and reflection in sputtered $CuScO_2$ films after each processing stage. From this data, the absorption coefficient, α, was determined, and the band gaps were determined by plotting $(\alpha E)^2$ vs. E. $Cu_2Sc_2O_5$ is very transparent with a value of about 90% for *T/(1-R)* in the visible spectrum and a direct band gap of 3.75 eV. $CuScO_2$ films are very transparent after the RTA processing with *T/(1-R)* averaging 85% in the visible region ($\alpha=2x10^4$ cm^{-1}) and a direct band gap of 3.6 eV. The $CuSc_{1-x}Mg_xO_{2+y}$ films become darker after intercalation, *T/(1-R)* is reduced to about 50% ($\alpha=7.5x10^4$ cm^{-1}) for the film intercalated at low oxygen pressure with the direct band gap remaining at 3.6 eV. The high pressure intercalation yields a value of *T/(1-R)* of only about 30% ($\alpha=1.5x10^5$ cm^{-1}). While the oxygen intercalation has a marked effect on the transparency, Mg doping does not negatively affect transparency at the doping levels tested here.

4 FILMS PRODUCED USING PULSED LASER DEPOSITION

4.1 Introduction and Experimental Procedure

$CuScO_2$ films were produced with a pulsed laser deposition system (PLD) at Oregon State University. PLD is a process in which a high-energy laser is focused onto a target so that material is ablated from the target and lands on the substrate on which the film is to be grown. The process is performed in a vacuum chamber to limit contamination and interference from gaseous species. Special reactant gases may be intentionally introduced during the deposition. The absorbed electromagnetic radiation from the laser beam is converted into electronic, thermal, and chemical energy to cause evaporation, ablation, excitation, plasma formation, and exfoliation. The ejected material creates a plume consisting of energetic atoms, molecules, electrons, ions, and clusters of molten globules [48]. A recent paper from the Technology Research Institute of Osaka reports that highly-oriented 3R $CuScO_2$ has been grown on single-crystal sapphire substrates at 925^{o}C substrate temperature using PLD and a $Cu_2Sc_2O_5$ target with no post-deposition annealing [41].

The OSU system uses a Lambda Physik Compex 201 KrF excimer laser at 248 nm. The energy density was 1.7 J/cm^2 with a 20 ns pulse, and a pulse repetition rate of 5 Hz. The deposition times varied from 10 to 20 minutes, and the number of shots varied from 3000 to 6000. Film thicknesses were measured to be between about 150 and 300 nm using these parameters. The chamber was pumped down to a base pressure of ~1x10^{-8} torr with a turbo-molecular pump backed by a dual rotary vane

mechanical pump. The chamber was filled with 99.997% O_2 to a deposition pressure of $5x10^{-3}$ Torr. The oxygen reacts with the evaporants to be incorporated into the growing film.

The target used was an undoped $CuScO_2$ sintered pellet 1" in diameter and 80% theoretical density. Substrates were heated to ~850^oC in 20 minutes using a quartz halogen lamp. These high substrate temperatures are much higher than the < 350^oC temperatures used for the sputtered films. Single-crystal sapphire substrates were used in an effort to make the films epitaxial. There is a relatively large lattice mismatch between the *a* lattice parameter of Al_2O_3 (4.76 Å) and the *a* lattice parameter of $CuScO_2$ (3.22 Å). However, it is the most similar single-crystal substrate that is hexagonal and is commonly available. The substrate-target distance was varied from 1" to 1.5" in an on-axis configuration. The films were intercalated in the same setup used for the sputtered films under high O_2 pressure of 800 p.s.i. ($4x10^4$ Torr) at 400^oC for 24 hours.

4.2 Results and Discussion

Fig. 4.1 shows the XRD patterns for as-deposited and oxygen intercalated films. Due to the data collection method used for this analysis the relative intensities are irrelevant because it relies on a polycrystalline structure. The films are 3R $CuScO_2$ after deposition so no post-deposition processing is required. The as-deposited films are insulating and mostly transparent with a light brown color. There are two small impurity peaks in both patterns that were not identified. They do not correspond to

Al_2O_3 or any of the Cu-Sc-O system phases. The same change in structure upon oxygen intercalation seen in the sputtered films is seen with the PLD films. The XRD patterns show how the peaks from planes that are not parallel to the *c*-axis split and shift to smaller *2θ* due to the crystal structure elongating in the *a*-axis direction. (In particular, note the (*110*) peak around 57° *2θ*. The shift corresponds to an increase in the *a* lattice parameter from 3.22 Å to 3.25 Å. This shift in the *a*-axis lattice parameter is an indicator of oxygen content. In bulk $CuScO_{2+y}$, the largest amount of oxygen results in *a*=3.26 Å and corresponds to y=0.5 [26]. Thus the PLD film is not fully oxygenated under the same conditions that the sputtered films were fully oxygenated. The reason presumably lies in the improved crystallinity and higher degree of orientation. This reduces grain boundaries, the primary means of oxygen diffusion in the intercalation process.

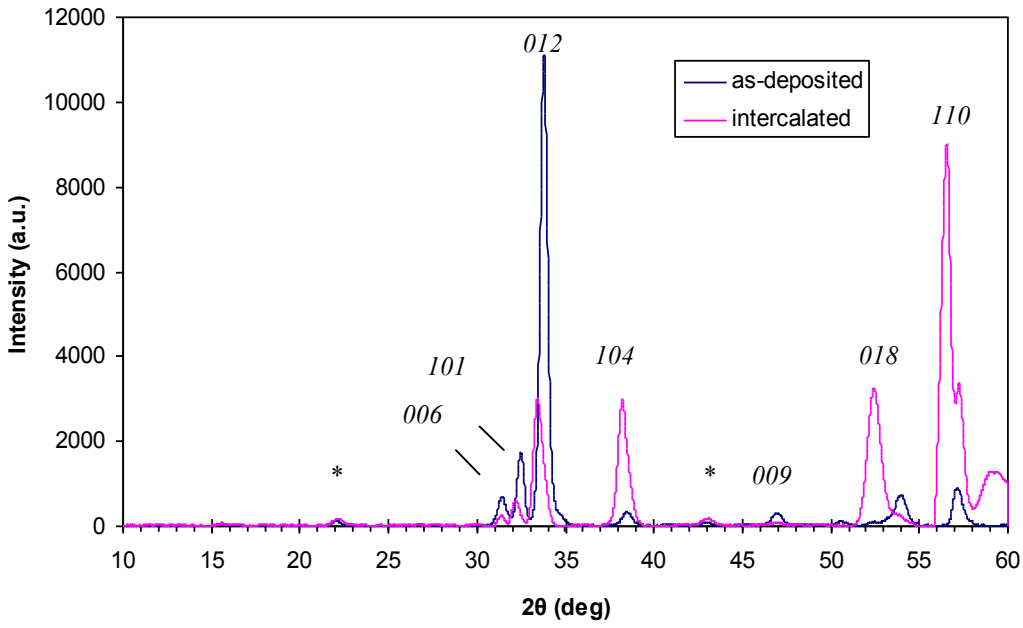

Figure 4.1 XRD patterns of as-deposited and intercalated $CuScO_{2+y}$ films produced using PLD. The small impurity peaks (*) are unidentified. All other peaks correspond to 3R $CuScO_2$ with *hkl* planes labeled.

The PLD films are highly oriented, or textured. The high degree of orientation is seen in the plot of the raw data collected at an incident angle of 12.5° in Fig. 4.2. *2θ* increases to the left of the crosshatch at 0° while χ is the radial direction. The polycrystalline sputtered film in Fig. 4.3 show a continuous curved line at a specific *2θ* at a single intensity for all values of χ. The large dark spot in this picture is attributed to the amorphous SiO_2 substrate. A polycrystalline material shows continuous lines because it contains many randomly oriented crystallites of which some will diffract for all values of χ. The elongated spots in the raw data signify that the film is highly oriented. Some spots from the Al_2O_3 substrate are also present in Fig. 4.2. These spots are very sharp and well-defined. The most intense spot is from the (*006*) plane, suggesting that the film is *c*-axis oriented.

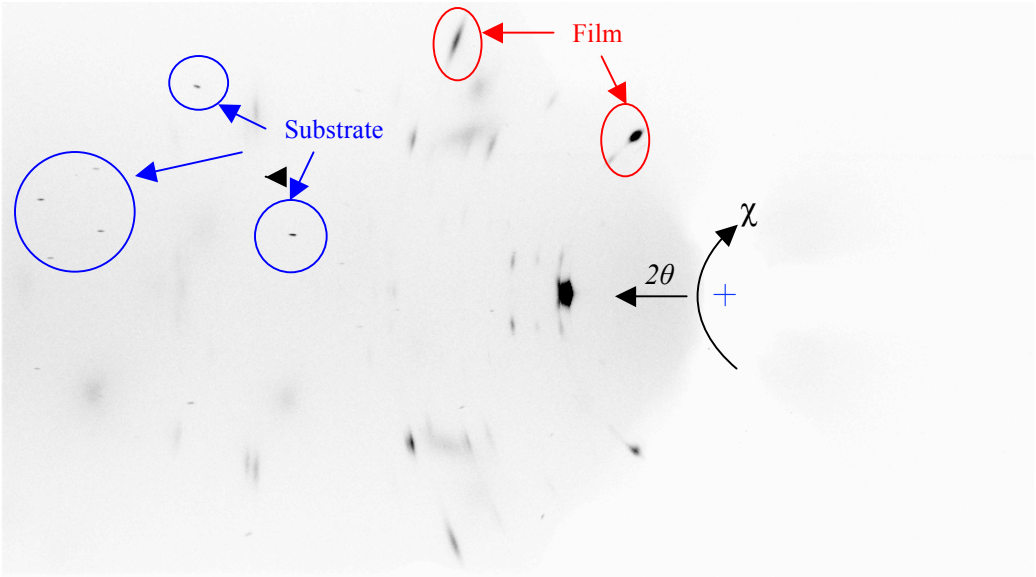

Figure 4.2 Raw XRD intensities of intercalated $CuScO_{2+y}$ film produced using PLD as a function of *2θ* and χ. The single crystal Al_2O_3 substrate has small, well-defined spots. The spots from the film signify orientation.

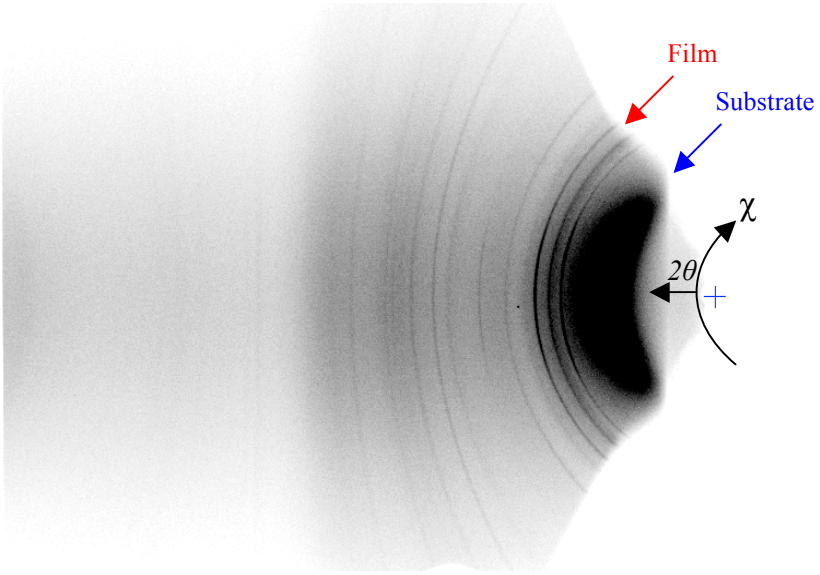

Figure 4.3 Raw XRD intensities of sputtered $CuScO_{2+y}$ film. The lines signify polycrystallinity. The large dark spot is from the SiO_2 substrate.

A pole figure is used to display structural orientation [28, 42]. With the film in a particular orientation, the incident beam is set to diffract from a specific set of planes (*i.e.* has a set value of θ) and the X-ray intensity measured for all angles of χ and Φ. Fig. 4.4 shows pole figures from the (*009*) and (*104*) planes. Since the (*009*) pole is normal to the surface of the film it can be stated that the film is strongly *c*-axis oriented. The (*104*) planes should show only three peaks because the 3R polytype has three-fold rhombohedral symmetry. The presence of six peaks indicates that there is twinning. The angle between the (*009*) and the (*104*) planes is 53°.

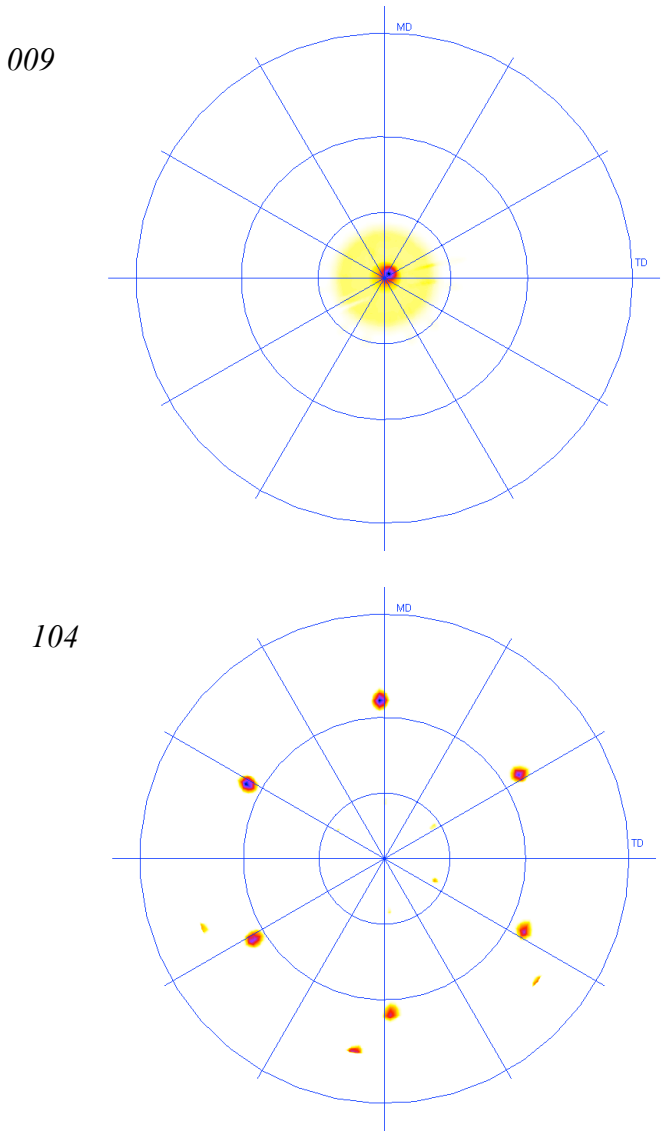

Figure 4.4 Pole figures for the (*009*) and (*104*) planes from the $CuScO_{2+y}$ film produced using PLD.

Atomic force microscopy (AFM) was performed to obtain information about surface morphology. Fig. 4.5 displays an AFM image with a 1x1 μm scan area for a film produced using PLD. The maximum height of the surface features (Rmax) is 76.8 nm, and the root mean square roughness (Rms) is 9.3 nm. The vertical scale in the image is 100 nm. The roughness of this film is twice as large as the sputtered films. Such roughness could be indicative of improved crystallinity since crystallites

grow normal to the film surface. The variation in surface height is over 25% of the total film thickness. This is very large and could present a problem if the film is to be used in a layered structure. However, modifying the deposition parameters such as substrate temperature, deposition pressure, and laser fluence has a major effect on the film quality, so the possibility exists for depositing smoother films and general optimization. A denser target usually results in a smoother film due to an inherent problem with PLD called "splashing" where large micron sized particles are ejected from the target and land on the film [49]. The features seen in the AFM image are probably too small to be attributed to splashing.

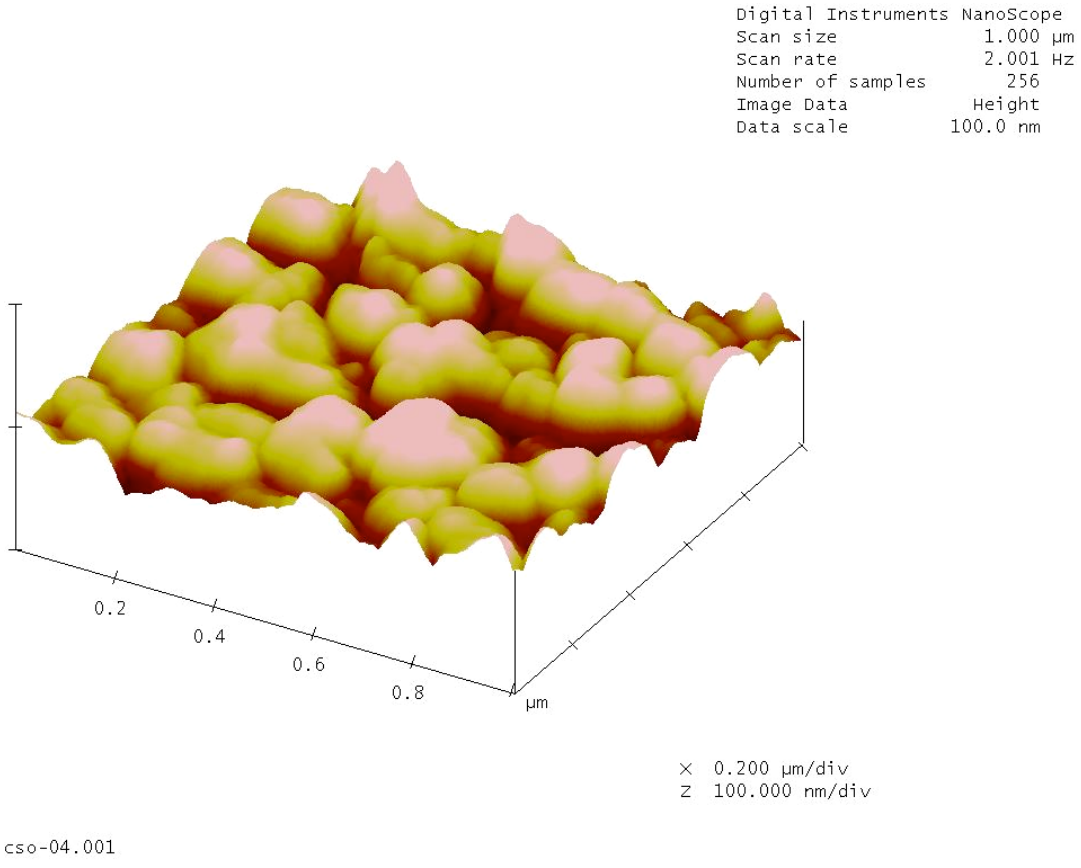

Figure 4.5 AFM image of $CuScO_{2+y}$ film produced using PLD. Rmax=76.8 nm, Rms=9.3 nm.

A room temperature conductivity of $6x10^{-2}$ S/cm was measured in the intercalated film. This value is about two orders of magnitude less than the sputtered films intercalated under the same conditions. This is expected since the oxygen incorporation is less effective for the reason given above. Since there is less oxygen, there are fewer carriers introduced into the material.

Optical measurements were performed in order to determine the transmission and reflection, absorption coefficient, and band gap for the PLD films. Fig. 4.6 displays *T/(1-R)* for the as-deposited and intercalated films 280 nm thick. As in the sputtered films, the transmission is drastically decreased from intercalation. The average value of *T/(1-R)* and α for the as-deposited film in the visible range are about 80% and $2x10^{4}$ cm^{-1}, respectively. This is comparable to the annealed, non-intercalated sputtered films. *T/(1-R)* for the intercalated film in the visible region is about 35% with an average absorption coefficient of $5x10^{4}$ cm^{-1}. Even though *T/(1-R)* is lower in the PLD film than the intercalated sputtered film, the optical absorption in the visible region is lower due to the differences in films thickness (the PLD film was 280 nm thick, while the sputtered film was only 100 nm).

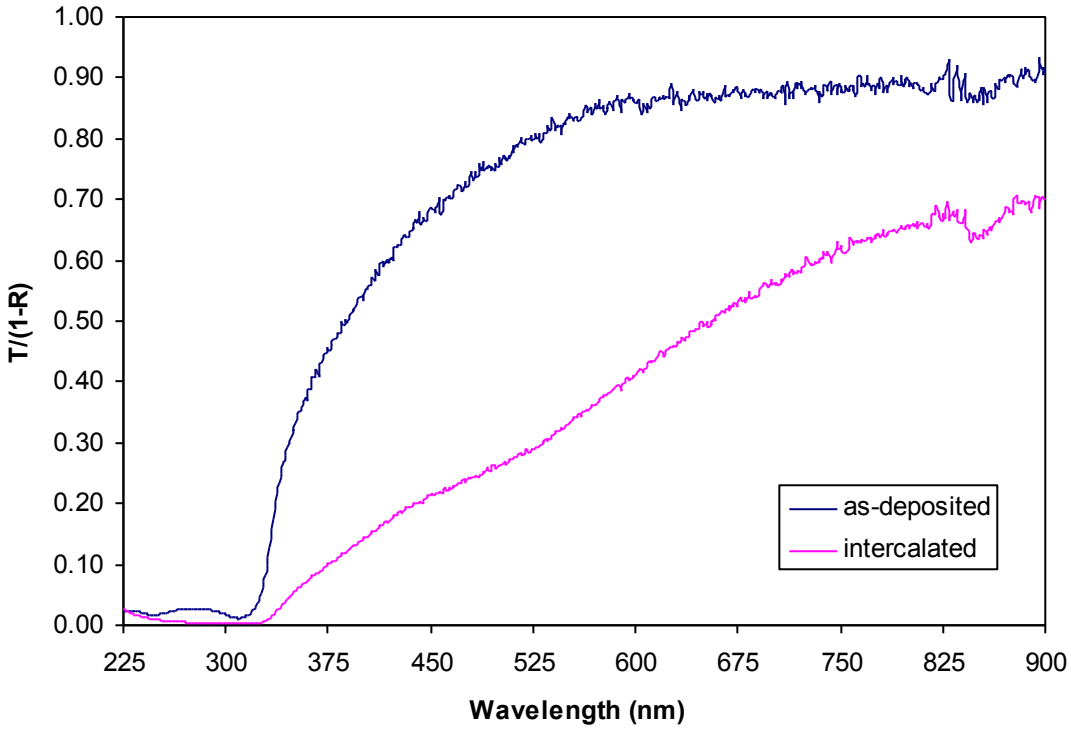

Figure 4.6 *T/(1-R)* for as-deposited and intercalated 280 nm thick $CuScO_{2+y}$ films produced using PLD.

The absorption coefficient for the sputtered films intercalated under low oxygen pressure (400 Torr) was $7.5x10^4$ cm^{-1}, while in the sputtered film intercalated at high oxygen pressure ($4x10^4$ Torr), $\alpha=1.5x10^5$ cm^{-1}. The increase in optical absorption is an indication of how much oxygen is being intercalated. The absorption coefficient for the sputtered film was three times higher than the PLD film intercalated under the same conditions. This is a further indication that less oxygen is being intercalated in the PLD film compared to the sputtered film.

In order to determine the direct band gap $(\alpha E)^2$ vs. E is shown in Fig. 4.7. A value of 3.7 eV is obtained for the as-deposited film, while a value of 3.6 eV is obtained for the intercalated film. The direct band gap determined in the sputtered films was 3.6 eV. The reason for the higher band gap in the as-deposited PLD film is

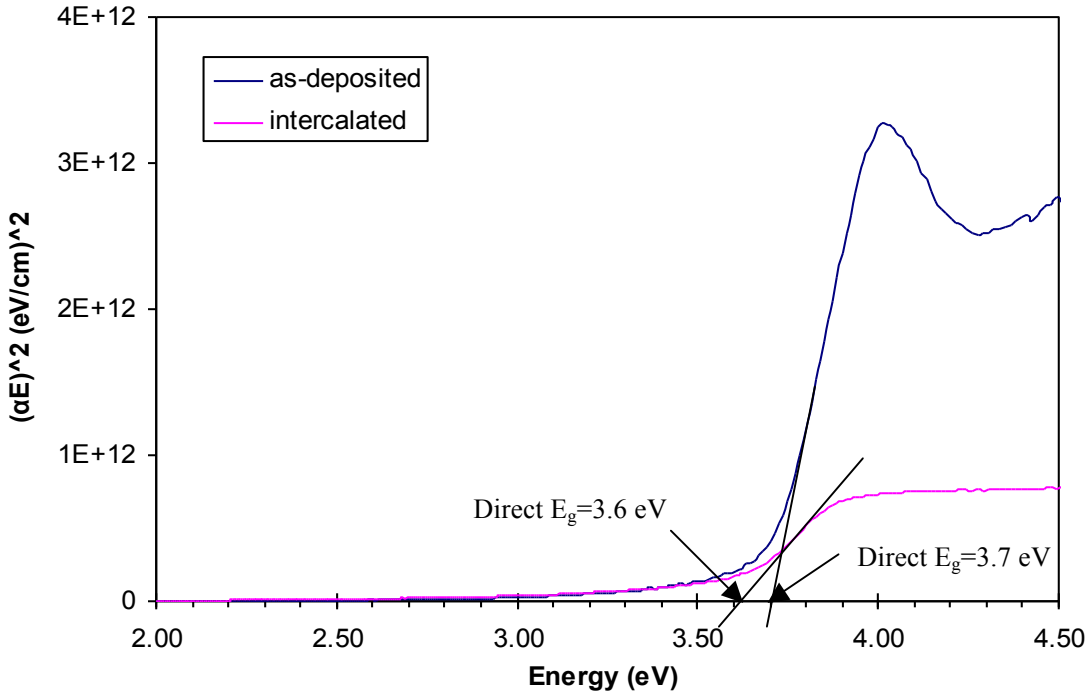

Figure 4.7 $(\alpha E)^2$ vs. E for an as-deposited and intercalated $CuScO_{2+y}$ film produced using PLD.

most likely because of the crystal structure being more defect free than any of the other films. The carrier states introduced from the intercalation and other defect states inherent in polycrystalline or amorphous material result in a reduction of the band gap, or the introduction of an interband impurity state or trap state. A perfect crystal will have sharp, well-defined energy bands. Defect states usually "smear out' the band gap because the edges of the bands tail off instead of sharply falling off and this can cause the gap to decrease.

4.3 Conclusion

$CuScO_2$ films produced on Al_2O_3 substrates using PLD are highly oriented after deposition and the crystallite size is presumably larger than in the sputtered films. The large oriented crystallites also make it more difficult for oxygen intercalation because there are fewer grain boundaries for the oxygen to diffuse into the film. The conductivity achieved was over two orders of magnitude less than the intercalated sputtered films (0.06 S/cm compared to 26 S/cm). As with the sputtered films, there is an elongation of the structure perpendicular to the *c*-axis. The surface of PLD films is very rough and unsuitable for multi-layered structures, but this can be improved with a refinement of deposition parameters. The band gap obtained through optical measurements for the as-deposited PLD film was slightly higher than that obtained for the intercalated PLD film. This could be an indication of the intercalation introducing a shallow acceptor state ~0.1 eV above the valence band. The band gap of the sputtered films was slightly less because the films were less oriented than the PLD films. The defect states "smear out" and effectively reduce the band gap. This "smearing out" is a tailing off of the bands as opposed to an introduced interband impurity state or trap state.

5 DISCUSSION

One of the more important results of this study is that it was determined that the Mg is an effective dopant, but the oxygen intercalation has a much larger effect on the conductivity. The large difference between the two doping techniques (oxygen intercalation and Mg doping) can be explained by the number of dopants that each one generates. According to the EMPA results, the maximum amount of Mg incorporated into the films made from the 15% Mg target was about x=0.05 in $CuSc_{1-x}Mg_xO_{2+y}$. It is difficult to discern the maximum amount of intercalated oxygen from the EMPA results, but other studies on the bulk powder form of the material have found that the maximum amount for y is 0.5 [26]. When one Mg^{2+} ion substitutes for one Sc^{3+} ion there is one hole generated. When an O_2 molecule dissociates and enters the film each O atom will want to react to form the more energetically favorable O^{2-}. When an O atom is incorporated interstitially it takes an electron from two adjacent Cu^{1+} ions and oxidizes them to Cu^{2+}. In this process two holes are generated for each oxygen dopant.

In a collection of 100 $CuSc_{0.95}Mg_{0.05}O_{2.5}$ molecules there will be five holes generated by the Mg, and 100 holes generated by the excess oxygen. According to this idealized model the oxygen intercalation results in 20 times the amount of carriers over the Mg doping. Unrealistically assuming 100% doping efficiency, this translates to a carrier concentration of 8.5×10^{20} cm^{-3} from the Mg doping and 1.7×10^{22} cm^{-3} from the oxygen intercalation. At these very high carrier concentrations it can

be stated that the reason the conductivity is so low is because of an extremely low hole mobility.

The conductivity of a hole majority carrier material is given by $\sigma=pq\mu_p$ where p is the hole concentration (cm^{-3}), q is the electron charge ($1.6x10^{-19}$ C), and μ_p is the hole mobility ($cm^2/V\cdot s$). Generally, hole mobility is consistently lower than electron mobility in a semiconductor. It is possible that the two doping techniques in this material give different hole mobilities.

Attempts to measure the Hall mobility on the films in this research were not successful due to the dc Hall voltage being too small to measure. This suggests that the hole mobility in $CuScO_2$ is less than 0.5 $cm^2/V\cdot s$. Lower limits, based on the measured conductivity and ideal carrier concentrations, can be set at about $1.5x10^{-4}$ $cm^2/V\cdot s$ for Mg doping and $9.6x10^{-3}$ $cm^2/V\cdot s$ for the oxygen intercalation. It is likely there is a compensation or trapping effect so that 100% doping efficiency is not accomplished. The mobility is very small in comparison to the room temperature hole mobility of highly doped Si of about 100 $cm^2/V\cdot s$ [39], and a measured Hall mobility of about 20 $cm^2/V\cdot s$ in ZnO:Al [2]. It should be noted that the mobility can be defined in several different ways including effective mobility and Hall mobility.

It is possible to increase the Mg doping to levels greater than x=0.05 in $CuSc_{1-x}Mg_xO_2$. According to the sputter target XRD results, the solubility limit of the Mg is approached around x=0.15. Past this point, the Mg would segregate as MgO, which is an insulator and would be detrimental to conductivity. However, the films are made under non-equilibrium conditions so behavior different than the bulk powder form of the material may be observed, and it could be possible to stabilize Mg

in films at $x > 0.05$. Also, the conductivities of the annealed, non-intercalated films made from the 15% Mg target were actually less conducting that the films made from the 5% Mg target. This may be because of a decrease in carrier mobility due to scattering from ionized or neutral impurities.

Another reason the Mg is not as effective as a dopant is that it might be difficult for the holes generated by doping to migrate to the Cu sites. It is believed that the conduction occurs predominantly by variable range hopping where holes hop from one localized Cu site to an adjacent one along the Cu planes. So if the holes from the Mg doping are localized around the MO_6 octahedra they would not prove to be effective dopants. This is equivalent to saying that the effective hole mobility from the Mg doping is lower than the effective hole mobility from the oxygen intercalation. Alternatively, it is possible that the conduction path is different with Mg doping. Instead of Cu-Cu hopping, Cu-O-Mg-O-Cu linkages may provide a path for the holes [26].

It is not completely understood why substrate temperature during film deposition has an effect on conductivity. It could be due to the films retaining a higher degree of amorphous structure at lower substrate temperatures. The films deposited at lower substrate temperatures could have a finer crystallite size after annealing than the films deposited at higher substrate temperatures because they are slightly less oriented in the as-deposited state. Crystallite size increases during annealing, and if the crystallite size is larger to begin with before annealing it will increase even more after annealing. The oxygen intercalation requires grain boundaries to diffuse into the film. A higher crystallinity means fewer grain boundaries, and this could make it

more difficult for oxygen to enter the film. This trend is confirmed by comparing the PLD films to the sputtered films. The PLD films are highly oriented with large crystallites, whereas the sputtered films consist of many small crystallites. The intercalated sputtered films are two orders of magnitude more conductive than the films produced by PLD and intercalated under the same conditions. This is most likely because it is more difficult for oxygen to enter the film via grain boundaries.

Amorphous films could result in a slightly reduced band gap due to bond overlap. On the other hand, the scattering from defects is also greater in amorphous materials compared to crystalline materials so this would serve to decrease the hole mobility. It was not determined if the as-deposited films deposited at 350^{o}C are more crystalline than films deposited at 150^{o}C, and they do undergo the same high-temperature annealing which could negate the effects of substrate temperature. X-ray data of films deposited at different substrate temperatures proved inconclusive.

It is not definitively known whether or not the as-deposited sputtered films were $CuScO_2$. They are amorphous, but it is difficult to characterize films with no crystallinity. X-ray diffraction cannot be used because there are no lattice planes for diffraction, and electron microprobe analysis only gives information about stoichiometry, not what phases are present. Maybe the ion oxidation states and coordination is not consistent throughout the material. The annealing procedures used in this experiment assure the formation of $CuScO_2$. $CuScO_2$ is metastable at room temperature so it will only form when subject to high temperature processing under equilibrium conditions. But films are made under non-equilibrium conditions, so it is possible that it could be formed at lower temperatures.

6 CONCLUSION

The results of this research have illuminated several facets of the $CuScO_2$ system that were previously unknown. First and foremost, the effect of the Mg dopant on film properties was finally quantified. Mg does contribute holes to the system, but it cannot be incorporated in large enough quantities to produce the same conductivity as oxygen intercalation. On the other hand, at the levels of incorporation, the transparency is not compromised.

Using XRD, the processing steps were clarified and the formation of the intermediate $Cu_2Sc_2O_5$ phase was shown. The band gap of $Cu_2Sc_2O_5$ was determined to be 3.75 eV, while the band gap of $CuScO_2$ and $CuScO_{2+y}$ was determined to be 3.6 eV. XRD also revealed that the $CuScO_2$ films were polycrystalline and that the oxygen intercalation increases the *a* lattice parameter. The original non-intercalated films show an *a*-axis lattice parameter of 3.22 Å, and the intercalated films show an *a*-axis lattice parameter of 3.26 Å. An intermediate value of 3.24 Å was also found for a film intercalated at low oxygen pressure. In addition to the shifted peaks, the intercalated film peaks split, with a remnant of the original pre-intercalated position corresponding to a non-intercalated phase. This shows that the intercalated films do not intercalate homogeneously; they consist of a heavily oxygenated phase and a lightly oxygenated phase. This effect also makes it difficult to lightly intercalate films. Films intercalated for short times are usually spotty with some dark areas that have been intercalated, and other lighter areas that are not intercalated.

AFM showed that grain growth occurs during annealing, as evidenced by the increase in surface roughness, and that the surfaces of the films show a significant variation in morphology. It was shown with EMPA that the dopant concentration in the target is reproduced in as-deposited films, but annealed films contained only about $^1/_3$ the Mg content as the targets. A significant amount of the Mg is lost during the high temperature annealing process probably due to segregation. However, the EMPA also suggests that the films are not stoichiometric. This contradicts the XRD data that show the films consist of polycrystalline 3R $CuScO_2$ with only some minor impurities. EMPA data that suggest a non-stoichiometric Sc/Cu ratio are likely due to error, because of unreliable O and Cu signals.

A major advantage of $CuScO_2$ is that its conductivity can be modulated through Mg doping and oxygen intercalation by up to six orders of magnitude, from about 10^{-5} to 10^{1} S/cm. For the non-intercalated films, the ones made from the undoped target have a conductivity of 10^{-5} S/cm, whereas the ones made from the Mg doped targets have a conductivity of 10^{-3}-10^{-2} S/cm. The highest conductivity for the non-intercalated films is 0.026 S/cm made from the 5% Mg target. At intermediate intercalation there is also a trend seen with the Mg doping with the films made from the highly doped target being the most conductive at 9 S/cm. The highest conductivity in the fully-intercalated films is 26 S/cm with no large difference between the Mg doped and undoped films.

$CuSc_{1-x}Mg_xO_{2+y}$ can therefore be customized to different applications requiring varying levels of conductivity and transparency. The conductivity and transparency are inversely related when oxygen intercalation is used to induce conductivity. This

is because as more carriers are generated that are available to conduct a current, more photons from the incident light will also be absorbed.

The PLD films were much more crystalline than the sputtered films due to the higher substrate temperature during deposition and the use of single crystal sapphire substrates. AFM revealed that the PLD films have much rougher surfaces than the sputtered films, which could be evidence of the higher degree of crystallinity. The PLD films could not be intercalated as successfully as the sputtered films. The conductivity of the intercalated PLD film was only 0.06 S/cm, two orders of magnitude less conductive than the intercalated sputtered films. This is because of the fact that the oxygen requires grain boundaries to diffuse into the film. The absence of grain boundaries in the highly oriented PLD films renders them less penetrable by the oxygen.

The high processing temperatures used in the production of these films might also make them undesirable for use in large-scale production. High temperatures translate to high energy consumption and higher costs, which is of course undesirable from a manufacturing standpoint. Additionally, the high processing temperatures make it extremely difficult to produce a device where $CuScO_2$ is not the base layer. The high temperature anneal in the case of the sputtered films and the high substrate temperature in the case of the PLD films will likely have a large effect on the other materials in the device from diffusion, grain growth, and phase changes.

There is a tradeoff between the increase in intrinsic conductivity achieved with higher crystallinity due to fewer scattering centers and the increase in conductivity from the shallow defects present in the crystal structure. Grain boundary scattering

and ionized impurity scattering both decrease the mobility. But defects in this material are necessary for conductivity. There is also a decrease in conductivity seen with the smaller amount of oxygen intercalation possible in films of higher crystallinity. A perfect $CuScO_2$ crystal would be insulating and colorless assuming the indirect transition is truly suppressed or non-existent.

With this in mind, it is suggested for further research to explore other possibilities with producing films using PLD. The major advantage is that films can be made *in-situ* with no post deposition annealing. First of all, it would be beneficial to produce heavily Mg-doped films by PLD on sapphire at high processing temperatures. With fewer grain boundaries, the holes from the Mg would experience less scattering. Mg does not negatively affect transparency at low doping levels, but it is possible that it could affect transparency at higher levels.

It would be useful to precisely determine the doping levels (both Mg and O) in the films. The EMPA system used for this analysis is currently being updated with newer, more powerful software that will be better capable of analyzing the content of these films. It would also be useful to find out if what happens to the Mg that is present in the as-deposited sputtered films. Does it segregate from $CuScO_2$ during the RTA process? What is the maximum level of Mg doping that can be achieved in films? It is possible that the solubility limit of Mg in $CuScO_2$ is higher than x=0.05, especially when deposited under non-equilibrium conditions.

Another useful path could be to attempt to produce less crystalline films with the PLD at lower substrate temperatures. The films would need to be somewhat crystalline so that acceptable transparency is obtained, but with small enough

crystallites so that they can be intercalated easily. If polycrystalline films of $CuScO_2$ could be produced at substrate temperatures probably somewhere in the range of 500-800^oC this would be a step forward in terms of ease of processing and lower production costs. PLD also provides another advantage in that films can be deposited in 10 to 15 minutes for a typical 200 nm thick film compared to 2 hours with sputtering. It would also be beneficial to deposit smoother films. This can likely be accomplished with a denser target, a lower laser energy density, a lower substrate temperature, and by modifying some of the other deposition parameters (oxygen pressure, substrate-target distance, pulse rate, etc.)

So is there any hope for *p*-type transparent semiconductors? At this point, research on the various delafossite compounds has been done quite extensively, and it appears that with these materials it will not be possible to approach the conductivities seen in the highly conductive *n*-type compounds. This problem is an inherent materials property with electrons in the conduction band being more mobile than holes in the valence band in most semiconductors. It is possible to use these materials for specialized applications in which their conductivity is appropriate. For example, it was thought that $CuScO_2$ would be a good candidate to replace CuSCN as the solid hole semiconductor in a ZnO based dye-sensitized solar cell [43].

The possibility exists of finding other compounds with better properties. Alternative oxide-based and some sulfide and selenide-based compounds such as $BaCu_2S_2$ [44], $SrCu_2O_2$ [45], LaCuOQ [46] and BaCuQF:K [47] (Q=S, Se) have been explored as candidate *p*-type semiconductors. $BaCu_2S_2$ seems promising with a conductivity of 17 S/cm and average visible transparency of 70% in the visible

spectrum for a 430 nm thick film, somewhat improved over $CuScO_2$. However, the band gap for this material is only 2.8 eV so it is impossible to make it completely transparent. The addition of fluoride in this system to form BaCuSF extends the band gap, but also lowers the conductivity. Band gap modulation from 2.7 to 3.1 eV was accomplished in this material by substitution of Sr for Ba, and Se and Te for S [47]. The search for new materials will continue while applications are found for existing materials.

BIBLIOGRAPHY

1 R.G. Gordon, MRS Bulletin, Vol. 25, No. 18, 52-57 (2000).
2 T. Minami, *MRS Bulletin*, Vol. 25, No. 18, 38-43 (2000).
3 A. Kudo, H. Yanagi, K. Ueda, H. Hosono, H. Kawazoe, *Applied Physics Letters*, Vol. 75, No. 18, 2851-2853 (1999).
4 S. Narushima, H. Mizoguchi, K. Shimizu, K. Ueda, H. Ohta, M. Hirano, T. Kamiya, H. Hosono, *Advanced Materials*, Vol. 15, No. 17, 1409-1413 (2003).
5 R.L. Hoffman, B.J. Norris, J.F. Wager, *Applied Physics Letters*, Vol. 82, No. 5, 733-735 (2003).
6 K. Nomura, H. Ohta, K. Ueda, T. Kamiya, M. Hirano, H. Hosono, *Science*, Vol. 300, 1269-1272 (2003).
7 B.J. Norris, J. Anderson, J.F. Wager, D.A. Keszler, *Journal of Physics D: Applied Physics*, 36, L105-107 (2003).
8 R.L. Hoffman, J.F. Wager, M.K. Jayaraj, J. Tate, *Journal of Applied Physics*, Vol. 90, No. 11, 5763-5767 (2001).
9 H. Yanagi, T. Hase, S. Ibuki, K. Ueda, H. Hosono, *Applied Physics Letters*, Vol. 78, No. 11, 1583-1585 (2001).
10 H. Yanagi, PhD dissertation, Tokyo Institute of Technology, 2001.
11 F.A. Benko and F.P. Koffyberg, *J. Phys. Chem. Solids*, Vol. 45, No. 1, 57-59 (1984).
12 G. Thomas, *Nature*, Vol 389, 907-908 (1997).
13 H. Kawazoe, M. Yasukawa, H. Hyodo, M. Kurita, H. Yanagi, H. Hosono, *Nature*, Vol 389, 939-942 (1997).
14 J. Tate *et al.*, *Thin Solid Films*, 411 (2002) 119-124.
15 R. Nagarajan, A.D. Draeseke, A.W. Sleight, J. Tate, *Journal of Applied Physics*, Vol 89, No 12, 8022-8025 (2001).
16 N. Duan, A.W. Sleight, M.K. Jayaraj, J. Tate, *Applied Physics Letters*, Vol 77, No 9, 1325-1326 (2000).
17 H. Yanagi, S. Park, A.D. Draeseke, D.A. Keszler, J. Tate, *Journal of Solid State Chemistry*, 175 (2003) 34-38.
18 M.K. Jayaraj, A.D. Draeseke, J. Tate, A.W. Sleight, *Thin Solid Films*, 397 (2001) 244-248.
19 H. Yanagi, S. Inoue, K. Ueda, H. Kawazoe, H. Hosono, N. Hamada, *Journal of Applied Physics*, Vol. 88, No. 7, 4159-4163 (2000).
20 M.S. Lee, T.Y. Kim, D. Kim, *Applied Physics Letters*, Vol. 79, No. 13, 2028-2030 (2001).
21 M. Trari, J. Topfer, J.P. Doumerc, M. Pouchard, A. Ammar, P. Hagenmuller, *J. of Solid State Chemistry*, 111, 104-110 (1994).
22 M. Elazhari, A. Ammar, M. Elaatmani, M. Trari, J.P. Doumerc, *Eur. J. Solid State Inorganic Chemistry*, 34, 503-509 (1997).
23 R.D. Shannon, *Acta. Cryst*., A 32, 751-767 (1976).
24 *U.S. Gun II: Owner's Operation and Maintainance Manual for the US Gun, Inc. Sputtering Source*, April 1997, 5.
25 CPDS-International Centre for Diffraction Data. Data files: 77-0199 (Cu_2O), 78-0430 (MgO), 72-0629 (CuO), 83-1256 ($Cu_2Sc_2O_5$), 77-2496 (2H $CuScO_2$), 79-

0599 (3R $CuScO_2$), 39-0244 (3R $CuYO_2$), 77-2493 (3R $CuAlO_2$), 77-2495 (3R $CuGaO_2$).
26 J. Li, A. Yokochi, A.W. Sleight, *Oxygen Intercalation of Two Polymorphs of $CuScO_2$*, November 2003 (to be published).
27 S. Park and D.A. Keszler, *Synthesis of 3R $CuMO_{2+\delta}$*, June 2002 (unpublished).
28 B.D. Cullity, *Elements of X-Ray Diffraction* 2nd Edition, Addison-Wesley Publishing Co., Inc., 1978.
29 R.C. Jaeger, *Vol. 5: Introduction to Microelectronic Fabrication*, Addison-Wesley Publishing Co., Inc., 1988, 73.
30 N.F. Mott, *Metal-Insulator Transitions*, Taylor & Francis LTD, London, 1974, 34-37.
31 N.F. Mott, *Conduction in Non-Crystalline Materials*, Clarendon Press, Oxford, 1987, 27-29.
32 M. Chen, Z.L. Pei, X. Wang, C. Sun, L.S. Wen, *Journal of Materials Research*, Vol. 16, No. 7, July 2001, 2118-2123.
33 D.C. Paine, T. Whitson, D. Janiac, R. Beresford, C.O. Yang, B. Lewis, *Journal of Applied Physics*, Vol. 85, No. 12, 8445-8450 (1999).
34 R. Kikinishi, B.C. Nielsen, J. Tate, J. Li, A.W. Sleight, *Structural and Transport Properties of $CuSc_{1-x}Mg_xO_{2+y}$ delafossites*, (submitted to *Phys. Rev. B* Feb. 2004).
35 L. Kilcher, *Optical Spectroscopy of Transparent Oxides from the UV to near-IR and a Method for Determining the Refractive Index of Transparent Thin Films*, Senior Thesis, Oregon State University, May 2003.
36 P.Y. Yu and Manual Cardona, *Fundamentals of Semiconductors: Physics and Materials Properties*, 3rd Ed. Springer-Verlag Berlin Heidelberg, New York, 2001, 268-276.
37 A. Buljan, P. Alemany, E. Ruiz, *J. Phys. Chem. B*, 1999, 8060-8066.
38 X. Nie, S.-H. Wei, S.B. Zhang, *Physical Review Letters*, Vol. 88, No. 6, 066405 (2002).
39 R.F. Pierret, *Semiconductor Device Fundamentals*, Addison-Wesley Publishing Co, Inc., 1996, 79-88.
40 C.M. Wolfe, N.H. Holonyak, Jr., G.E. Stillman, *Physical Properties of Semiconductors*, Prentice-Hall, Inc., 1989, Chp. 2.
41 Y. Kakehi, S. Nakao, K. Satoh, T. Yotsuya, *Thin Solid Films*, 445 (2003) 294-298.
42 U.F. Kocks, C.N. Tome, H.-R. Wenk, *Texture and Anisotropy*, Cambridge University Press, 1998.
43 B. O'Reagan, D.T. Schwartz, S.M. Zakeeruddin, M. Gratzel, *Advanced Materials*, 12, No. 17, 1263-1267 (2000).
44 S. Park *et al*., *Applied Physics Letters*, Vol. 80, No. 23, 4393-4394 (2002).
45 A. Kudo, H. Yanagi, H. Hosono, H. Kawazoe, *Applied Physics Letters*, Vol. 73, No. 2, 220-222 (1998).
46 H. Hiramatsu *et al*., *Applied Physics Letters*, Vol. 82, No. 7, 1048-1050 (2003).
47 H. Yanagi, J. Tate, S. Park, C.H. Park, D.A. Keszler, *Applied Physics Letters*, Vol. 82, No. 17, 2814-2816 (2003).
48 C.H. Park, D.A. Keszler, H. Yanagi, J. Tate, *Thin Solid Films*, 445 (2003) 288-293.

49 D.B. Chrisey, G.K. Hubler, *Pulsed Laser Deposition of Thin Films*, John Wiley & Sons, Inc., New York, 1994.
50 B.G. Yacobi, *Semiconductor Materials: An Introduction to Basic Principles*, Kluwer Academic / Plenum Publishers, New York, 2003, p. 52-60, 81-86.